Air Force Institute of Technology

AFIT Scholar

Theses and Dissertations   Student Graduate Works

3-3-2003

Spacecraft Charging at Geosynchronous Altitudes: Current Balance and Critical Temperature in a Non-Maxwellian Plasma

Jose T. Harris

Follow this and additional works at: https://scholar.afit.edu/etd

Part of the Plasma and Beam Physics Commons

SPACECRAFT CHARGING

AT GEOSYNCHRONOUS ALTITUDES:

CURRENT-BALANCE AND CRITICAL TEMPERATURE

IN A NON-MAXWELLIAN PLASMA

THESIS

Jose T. Harris, Captain, USAF

AFIT/GAP/ENP/03-05

SPACECRAFT CHARGING

AT GEOSYNCHRONOUS ALTITUDES:

CURRENT BALANCE AND CRITICAL TEMPERATURE

IN A NON-MAXWELLIAN PLASMA

THESIS

Presented to the Faculty

Department of Engineering Physics

Air Force Institute of Technology

Air University

Air Education and Training Command

In Partial Fulfillment of the Requirements for the

Degree of Master of Science (Applied Physics)

Jose T. Harris, B.S.

Captain, USAF

March 2003

AFIT/GAP/ENP/03-05
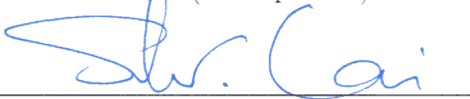
SPACECRAFT CHARGING
AT GEOSYNCHRONOUS ALTITUDES:
CURRENT BALANCE AND CRITICAL TEMPERATURE
IN A NON-MAXWELLIAN PLASMA

Jose T. Harris, B.S

Captain, USAF

Approved:

_____ _____
Devin J. Della-Rose (Chairperson)   24 Feb 03
                                    Date

_____ _____
Shu T. Lai (Member)   5 Mar 03
                                    Date

_____ _____
Aihua W. Wood (Member)   11 Mar 03
                                    Date

Preface

The secret of success is consistency of purpose.

Benjamin Disraeli

Service is a privilege I do not take lightly. A primary part of the service I am allowed to perform includes doing my part to protect our American way of life. This includes doing my best to see that the guy on the other side of the war front gets to be a hero. This has been my duty since I first entered the Air Force during the Cold War, and it is my duty now. I remind myself that this scientific endeavor has a military application or the Air Force wouldn't be paying me to carry it out. All the while, I'm also privileged to improve myself and extend my usefulness to the Air Force and my country. I'm thankful to the United States Air Force for the opportunity to serve my country in this and other capacities.

This is definitely the most scientifically noteworthy challenge I've ever taken up, and I hope that it proves successful. Any success achieved in this endeavor is largely due to the following:

Dr. Shu T. Lai of AFRL, who is among the pioneering researchers in the area of spacecraft charging, and whose work provides the bulk of the foundation upon which my work rests, offered the thesis topic. His suggested outline for approaching the problem was the basis for my methodology. Maj Devin J. Della-Rose, who is among the best academic instructors I've had the pleasure of learning from, guided me through the research process. He has been an encourager as he enthusiastically paralleled some of my research to gain insight into the problem. The time and effort he expended in helping me were critical for me to understand, define, and work through this research. Dr. Aihua Wood helped me sort out some of the critical mathematical issues, and her help with respect to limits and rates of convergence of the Kummer functions was especially crucial for broadening the applicability of the kappa current balance equation.

Table of Contents

vii

List of Figures

List of Tables

AFIT/GAP/ENP/03-05

Abstract

Spacecraft charging threatens to disable spacecraft components and adversely impact any satellite function. Electrostatic charge, and especially discharge, can hinder the proper operation of, or destroy, spacecraft components, thereby rendering the spacecraft ineffective or inoperative (Prokopenko and Laframboise, 1980:4125). The level of charging is dependent on the particle energy (speed) distribution. Current spacecraft design and materials provide limited protection against the dangers of electrostatic discharge, and active measures such as beam emission are also employed. The goal of this thesis is to investigate the kappa distribution as an alternative to the Maxwellian distribution as a method of predicting the onset of significant spacecraft charging by extending the research of Lai and Della-Rose (2001). Their work demonstrated the existence of critical (electron) temperatures above which the onset of significant spacecraft charging occurs. Below this critical temperature, significant charging does not occur (Lai and Della-Rose, 2001:927).

Space plasmas are known to exhibit non-Maxwellian distributions at high (> 10 keV) energies (Vasyliunas, 1968:2840), and this knowledge provides the motivation for extending the work of Lai and Della-Rose to the kappa distribution. Solving the current balance equation is central to this area of research. Data from Los Alamos National Laboratory scientific instruments onboard geosynchronous satellites were analyzed to determine the efficacy of the kappa approach. However, the results of this thesis suggest that the kappa distribution, though superior to the Maxwellian at modeling high-energy particles (electrons), may be no better at determining charging onset.

SPACECRAFT CHARGING
AT GEOSYNCHRONOUS ALTITUDES:
CURRENT BALANCE AND CRITICAL TEMPERATURE
IN A NON-MAXWELLIAN PLASMA

I. Introduction

1.1 Objective

The goal of this research is to refine the correlation of spacecraft charging at geosynchronous altitudes to a threshold temperature above which significant spacecraft charging can occur. Emphasis is placed on the accumulation of charge on the spacecraft surface (surface charging). In an effort to reach the stated goal, an analytical formulation of the current-balance equation using a kappa distribution will be accomplished. A numerical comparison of the theoretical results against observations will be used to evaluate the success of the approach.

1.2 Motivation

Spacecraft charging threatens to disable spacecraft components and adversely impact any satellite function. Electrostatic charge, and especially discharge, can destroy the functionality of components or components themselves, thereby rendering them ineffective or inoperative (Prokopenko and Laframboise, 1980:4125). Additionally, a local environment consisting of excess charge can interfere with data collection, causing measurements taken by spacecraft instruments to be misleading and giving rise to improper conclusions about the space environment (DeForest, 1972:659; Lai, 1999:3). Presently, spacecraft design and materials provide limited protection against the dangers of electrostatic discharge.

Environmental assessment and space weather event forecasting, including forecasts of operational impacts of space weather, are among the primary missions of Air Force Weather Agency space weather operations. Informing space systems operators of when and where spacecraft charging can occur with sufficient warning time can aid in minimizing adverse operational impacts such as permanent damage to space assets. Furthermore, post-event engineering assessments of satellite failures can be improved if we can tell the satellite operators that charging did (or did not) play a role in a given failure.

The current balance equation reveals the limiting conditions for which the current into a surface element equals the current out of the element. Outside of these conditions, the net current is nonzero – i.e., charging can occur. Thus, the solution of the current balance equation is central to solving charging-related problems.

1.3   Scope

This study aims to refine the process of determining the critical temperature for the onset of spacecraft charging by incorporating the kappa distribution solution of the current balance equation as noted above. This research will examine data from Los Alamos National Laboratory (LANL) instruments aboard United States Department of Energy satellites 1997A, 1994-084, and 1991-081 from the following time frames: March and April 1999; March, June, and September 2000. The time periods were selected to coincide with previous work by Lai and Della-Rose (2001) as an extension for a non-Maxwellian plasma environment.

Eclipse events and a coronal mass ejection (CME) event will be examined. These two types of events fit the common theme of previous research and so will be useful for comparison of results. When the plane of the satellite's orbit intersects the earth-sun line, the satellite will be eclipsed by the earth's shadow near local midnight. Spacecraft charging can result from various mechanisms. The mechanisms we will explore are charging due to ambient plasma (ions and electrons), secondary

and backscattered electrons, and photoelectrons as well as charging associated with combinations of these particles. In this analysis, only charging due to ambient ions and electrons combined with secondary and backscattered electrons will be modeled mathematically. Other types of charging include differential charging, beam charging, bootstrap charging, and mechanically induced charging. These latter types are outside the scope of this thesis.

II. Background

This chapter will describe key parameters associated with spacecraft charging at geosynchronous orbit (GEO). First, the plasmasphere, which GEO spacecraft encounter daily will be covered. This will be followed by a brief description of particles responsible for spacecraft charging along with their associated distributions and energies outside the plasmasphere, where significant spacecraft charging tends to occur. Then a brief introduction to spacecraft charging will be presented. Finally, various charging scenarios will be discussed. The convention adopted here will be to represent particle temperatures in terms of energy (eV) – i.e., $T = k_B T$., where $k_B = 1.3806568 \times 10^{-23}\,\mathrm{J\,K^{-1}} = 8.617385 \times 10^{-5}\,\mathrm{eV\,K^{-1}}$ is Boltzmann's constant.

2.1   Spacecraft Environment at Geosynchronous Altitudes

The following sections will describe environmental factors affecting spacecraft at GEO. First, we will examine the plasmasphere, which is not normally associated with significant charging. This will be followed by a description of particles that influence spacecraft charging, including number densities and distributions associated with each type of particle.

2.1.1   Plasmasphere.   The plasmasphere is a near-Earth region containing cold ($\sim 1\ eV$), dense plasma. Electron densities in the plasmasphere typically range from 10 to $10^4\ cm^{-3}$ (Su, et al., 2001:1185). It extends from the terrestrial ionosphere into space over ranges of about 1 to 7 R_E, where 1 R_E is the radius of the Earth (6370 km). If the spacecraft is within the plasmasphere, the relatively dense ($> 1.0\ cm^{-3}$) and cool ($\sim$ few eV) plasma can envelop the satellite. Charging in this region is often induced by the photoelectric effect, which typically results in potentials of only a few volts (DeForest, 1972:655, 659). This charging process is further explained in Section *2.2.2.2.* At the plasmapause, first noted independently by Carpenter (1963) and Gringauz (1963), electron densities tend to drop considerably. The location of

the plasmapause varies with the level of geomagnetic activity (Carpenter, 1963), and it can extend beyond geosynchronous altitudes during "quiet times" ($K_p < 2$). K_p is a logarithmic, planetary index (0 to 9) of the disturbance of the geomagnetic field, with higher values implying greater disturbances (Parks, 1991:512).

2.1.2 Plasma Densities at Geosynchronous Altitudes. Beyond the plasmapause, electron densities are typically about 0.1 to 3 cm^{-3} at geosynchronous altitudes depending on the local time of the spacecraft and the level of geomagnetic activity.

2.1.3 Gradient-Curvature Drift. At geosynchronous altitudes, a gradient-curvature drift induced by the Earth's magnetic field determines the directions of the electrons and positively charged ions (see, for example, Kivelson and Russell, 1995:310-312). This gradient-curvature drift causes electrons to flow eastward and ions to flow westward. Thus, even after local midnight, a GEO spacecraft may experience significant charging due to electron currents.

2.1.4 Key Particle Descriptions and Distributions. The following sections describe electrons from various sources as well as (positive) ions and their associated distributions and fluxes at GEO. These particles, and their distributions with respect to kinetic energy, dictate the charging environment of GEO satellites.

2.1.4.1 Ambient Ions and Electrons. Ambient ion and electron densities are approximately 0.1 to 1.0 cm^{-3} at GEO. With the injection of magnetotail plasma, the density can increase to approximately 3.0 cm^{-3} (Hastings and Garrett, 1996:69-70).

2.1.4.2 Photoelectrons. Photoelectrons are created when photons strike the spacecraft surface and impart enough energy to induce electron emission from the spacecraft surface. Typical photoelectron energy is only a few eV (Hastings

5

and Garrett, 1996:148; Lai, 1999:5). Since photon densities are very high, photoelectron densities will be proportionately large. The number of photoelectrons produced and their energies are largely dependent on spacecraft material properties and design (Hastings and Garrett, 1996:147-148). The number flux of photoelectrons tends to be much greater than that of ambient electrons.

2.1.4.3 Secondary and Backscattered Electrons. When electrons strike a spacecraft, they will either be reflected or absorbed. If they are of low enough energy, they will be reflected. The reflection coefficient is approximately 0.05 (Hastings and Garrett, 1996:148) – that is, most electrons are absorbed. When electrons are absorbed, they will either collide with other electrons and backscatter or produce secondary electrons (explained below). Backscattered electrons are primary electrons that are ejected after they penetrate the surface. These electrons typically have slightly lower energy than they had upon impact. Sternglass (1954:345,352-356) considered backscattered electrons as those emitted with energies greater than 50 eV, and he found their energies to be about $\frac{1}{2}$ of that of incident electrons for primary energies of 0.2 to 32 keV. For this discussion, backscattered electrons can be incorporated as a reduction factor for incident electrons (Hastings and Garrett, 1996:149,169-170). The probability that backscattered electrons are emitted is denoted by $\eta(\varepsilon)$. Sternglass considered emitted electrons with energies below 50 eV as secondary electrons, and this is the convention adopted here.

Secondary electrons are emitted when a primary, high-energy, electron penetrates the spacecraft surface and imparts enough energy to neighboring electrons that these neighboring electrons can escape. If the energy of the primary electrons is large enough, but not too large, secondary electrons may be ejected. Also, energy from the primary electron may be imparted to more than one neighboring electron. So it is possible, even probable over some energy ranges, that the number of secondary electrons leaving the spacecraft surface is greater than the number of incoming – i.e., $\delta(\varepsilon) > 1$, where $\delta(\varepsilon)$ is the probability of secondary electron emission.

Figure 1 illustrates the dependence of secondary and backscattered electron emission on the primary energy of electrons impacting the spacecraft surface composed of non-activated CuBe with normal incidence. Secondary and backscattered yield curves are based on data fits derived by Sanders and Inouye (1978) and Prokopenko and Laframboise (1980), respectively. Note that in this example, $\delta(\varepsilon) = 1$ for primary electron energies of about 0.05 and 1.42 keV. Observe that $\delta(\varepsilon) < \eta(\varepsilon)$ up to about 10 eV, and that the sum $\delta(\varepsilon) + \eta(\varepsilon)$ approaches a constant (0.31) as the primary energy approaches 10 keV.
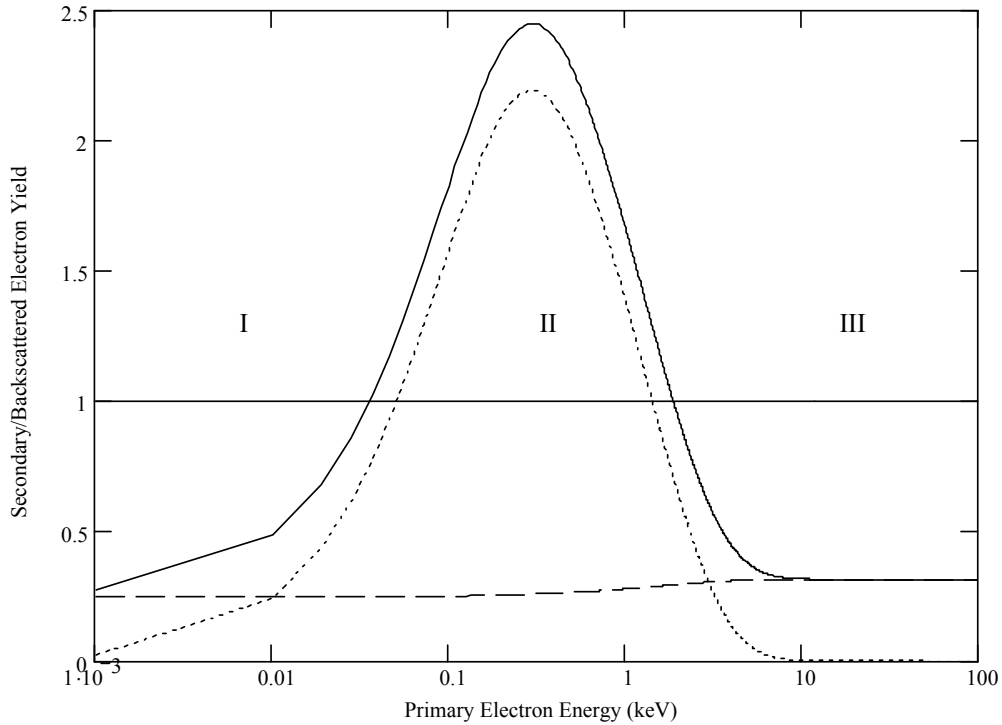
Figure 1   Secondary (δ_e - dot), backscattered (η_e - dash), and $\delta_e + \eta_e$ (solid) electron emission coefficients due to normal incidence of primary electrons on a surface composed of non-activated CuBe vs. primary electron energy ε.

2.2   Spacecraft Charging

Garrett (1981:577-579) gives an historical overview of spacecraft charging and related research up to 1981. He characterizes associated research into four distinct periods, beginning with the use of the Langmuir probe. He notes, "The first example of a spacecraft charging effect is in a paper by Johnson and Meadows [1955]." Large negative potentials ($-20\ kV$) were observed in eclipse on Applications Technology Satellite 6 (ATS-6) (1981:578) in the 1970's. Such potentials are characteristic of particle distributions that are well represented by the kappa distribution. DeForest (1972) was the first to note spacecraft charging at GEO.

Spacecraft charging is the buildup of potential on a spacecraft relative to that of the ambient (surrounding the spacecraft) plasma. By convention, the potential of the ambient space plasma is taken to be zero. When the spacecraft potential is nonzero relative to the space plasma, the spacecraft is charged. Spacecraft charging includes, but is not limited to, surface charging, frame charging, differential charging and deep dielectric charging. It is induced by a local difference in ion and electron fluxes (Lai, 1999:4), and most GEO spacecraft often charge to about $0.2 - 1\ keV$. (Hastings and Garrett, 1995:149; Lai, 1999:5).

Negative charging is predominant since the electron flux is about two orders of magnitude greater than the ion flux. This is a natural consequence of the differences in magnitude of the particle masses – i.e., if the electron and ion energies are assumed to be approximately equal, then the ratio of the electron velocity to the ion velocity is approximately equal to the inverse square root of the ratio of the ion mass to the electron mass. Therefore, in a quasi-neutral gas, the particle flux ratio varies as the ratio of the particle velocities.

2.2.1   The Thick Sheath Limit.   When examining spacecraft charging at GEO vs. low- or middle- Earth orbit, it is important to note the distinction between thin and thick sheath limits. Hastings and Garrett define the sheath as the region

"near the spacecraft surface where the quasi-neutrality [of the plasma] is violated" (1996:32). Within the sheath region, ions and electrons respond to one another as though they are not in a plasma. The critical value for the sheath thickness is called the Debye length, which is defined as

$$\lambda_D = \sqrt{\frac{\varepsilon_0 T}{n_0 e^2}} \tag{1}$$

where $e = 1.60217733 \times 10^{-19} C$ is the charge on a singly charged ion $(+e)$ or electron $(-e)$.

In the thin sheath limit, the Debye length is smaller than the characteristic dimensions of the spacecraft. On the other hand, for the thick sheath limit, the opposite holds true. Hastings and Garrett (1996:157) point out that spacecraft less than 10 meters in diameter will be subject to the thick sheath limit at GEO, where the Debye length is roughly 300 meters. This $(300\ m)$ estimate assumes a Maxwellian temperature $T_M = 1.0\ keV$, electron density $n_0 = 0.5\ cm^{-3}$. Inside the sheath, the plasma is non-neutral (Lai, 1999:3). In the thick sheath limit, every particle is independent so conservation of energy and angular momentum determine which particles will reach the spacecraft surface. Therefore, the sheath limit is important since this limit determines the influences on spacecraft charging at GEO.

2.2.2 Surface Charging Scenarios for GEO Spacecraft. Four common charging scenarios related to GEO spacecraft are presented. These include charging due to ambient ions and electrons, charging due to ambient ions and electrons plus photoelectrons, ambient ions and electrons plus secondary electrons, ambient ions and electrons plus photoelectrons and secondary electrons. This will provide an introduction to factors central to developing the current balance equation for GEO spacecraft.

2.2.2.1 Ambient Ions and Electrons. First we will examine the ambient ion and electron charging environment while neglecting photoelectrons and secondary and backscattered electrons. To begin, we determine whether the spacecraft will charge positively or negatively, if at all. Consider the flux, $\Gamma = nu$, of ions and electrons at zero spacecraft potential, where u is the particle (electron or ion) velocity, and suppose that $n_e = n_i$ as for a quasi-neutral plasma. Since $m_e << m_i$, if we assume that the ion and electron energies are approximately the same, then $u_e >> u_i$, so the electron flux is much greater than the ion flux, and the electron current causes the spacecraft to accumulate a negative charge, which will eventually serve as a potential barrier to incoming electrons, as well as enlarge the ion current.

Now to determine how much the spacecraft charges, we seek an equilibrium state where the net flux—and therefore the net current—is zero. Without loss of generality, consider that the spacecraft charges to some negative potential, V_{sc}, resulting in a potential barrier with energy, eV_{sc}. Incoming electrons with kinetic energy, $T < eV_{sc}$, will not be able to penetrate the barrier. So the number flux of electrons is limited, and an equilibrium state is achieved once the number flux of ions and electrons is equal. Note that the thermal energy of the electrons (electron temperature) is pivotal to determining how much charge will accumulate (Hastings and Garrett, 1996:168).

2.2.2.2 Ambient Ions and Electrons and Photoelectrons. Now consider the case of the spacecraft in sunlight (without regard for secondary and backscattered electrons). This can result in large numbers of photoelectrons being emitted from the spacecraft.

Recall that the number density of photoelectrons is much greater than that of ambient electrons. This results in a net positive charge about the sunlit surface. Since photoelectrons are directed away from the spacecraft, the resulting net positive potential will serve to attract escaping photoelectrons. However, photoelectron

energy is typically only a few eV, so the total charge about a sunlit surface typically can reach only a few volts positive.

Figures 2 and 3 illustrate the dependence of potential on temperature and are prime examples of the distinct differences between charging in sunlight vs. charging in eclipse. Notice that when the spacecraft is in eclipse it can reach much larger potentials than when it charges in sunlight. Measurements are from LANL 1994-084 data on 14 Mar 1999, and spacecraft local time is approximately six hours later than UT. The period of eclipse is highlighted in Figure 2 by the line at -2 kV. Also evident in Figure 3 is a threshold temperature for significant charging to begin. The determination of eclipse periods is described in Appendix A.
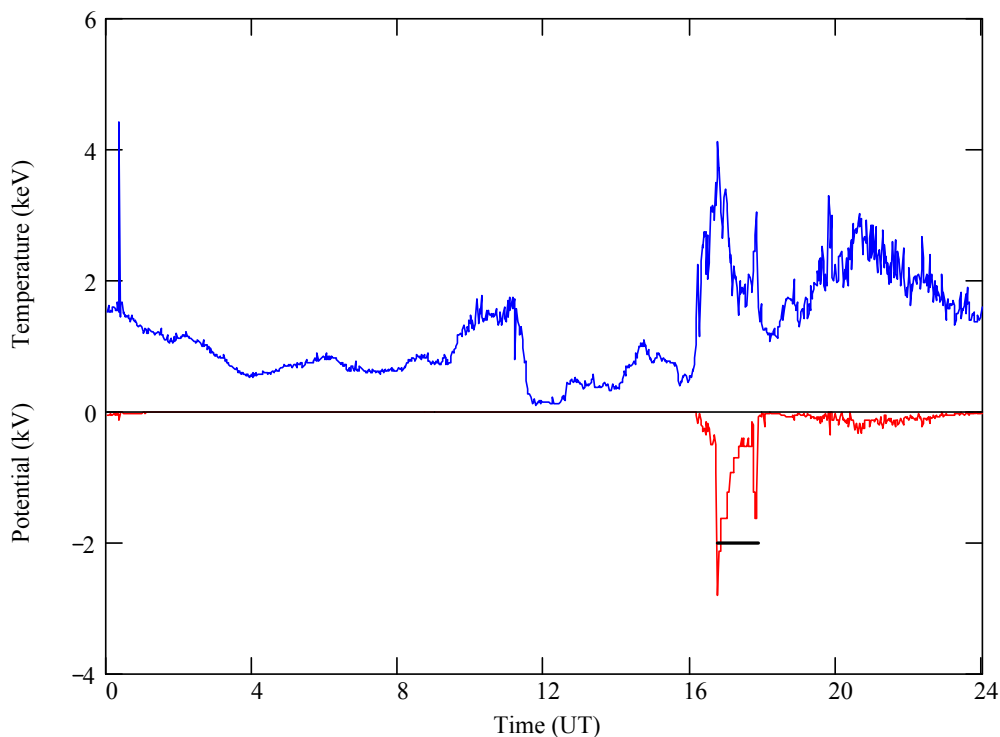
Figure 2   Correlation Between Spacecraft Potential and Electron Temperature from LANL 1994-084 Measurements Taken on 14 March 1999. The line at -2 kV highlights the period of spacecraft eclipse. (Data courtesy of Michelle F. Thomsen, Los Alamos National Laboratory.)

11
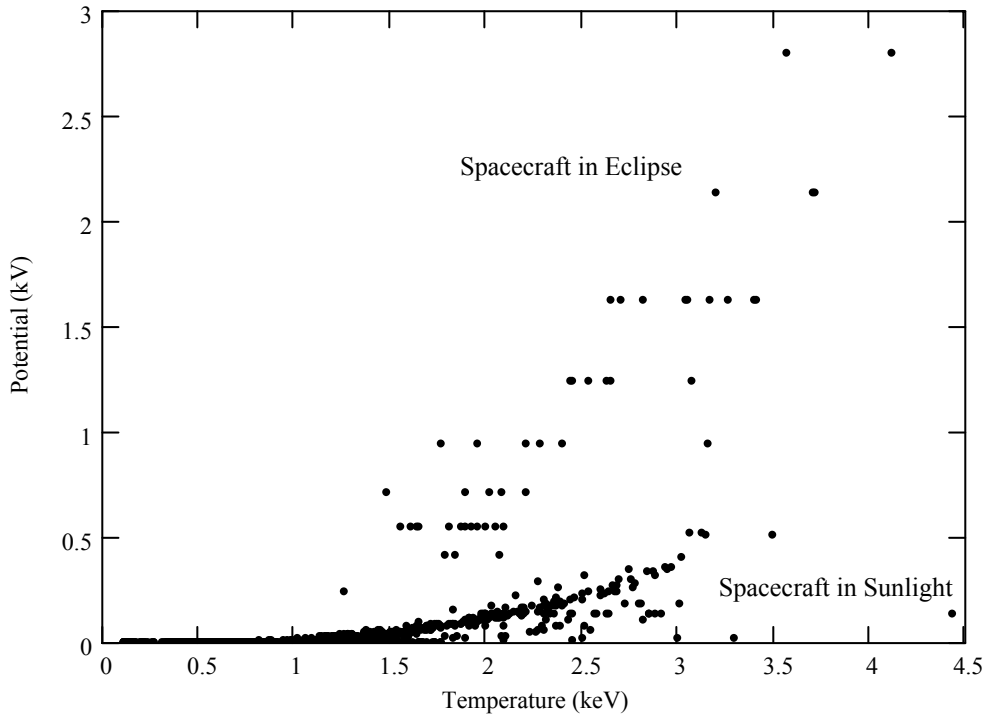
Figure 3   Spacecraft Charging in Sunlight vs. Charging in Eclipse as Determined
from LANL 1994-084 Measurements Taken on 14 March 1999. (Data
courtesy of Michelle F. Thomsen, Los Alamos National Laboratory.)

2.2.2.3 Ambient ions and electrons and secondary electrons.   As an
introduction, this discussion will cover a monoenergetic energy distribution of the
ambient electrons and ions. The case of an energy distribution over a range of
energies is presented in Section 2.6. Recall that backscattered electrons serve as
a scaling factor for the incident electron flux, and so they are absorbed into the
ambient electron flux term.

Now consider the three regions I, II, and III of in Figure 1 (ignoring the contri-
bution of photoelectrons), where the regions are delimited according to the secondary
electron yield (dotted line). In region I, the primary energy is too low to force emis-
sion of more electrons than are incident on the surface. That is, the incoming flux
will be greater than the outgoing flux, but with low kinetic energy less than that
of the first crossing where $\delta(\varepsilon) = 1$, and the electron current causes the spacecraft

12

to accumulate a negative charge dependent on the ambient plasma electron temperature (Rubin, et al., 1980:9). For a monoenergetic beam, the maximum potential attained will be no greater than the voltage equivalent corresponding to the $\delta(\varepsilon) = 1$ energy at the region I boundary.

In region II, the energy of the primary electrons is in the range where the number of secondary electrons produced exceeds the number of incident electrons, so the incoming flux of electrons will be less than the outgoing flux. Therefore, the secondary electrons will determine the amount of spacecraft charging, which will be positive with a potential corresponding to the energy of the outgoing secondary electrons. Since secondary electrons are of relatively low energy, the overall potential is typically not substantial.

In region III, the primary energy is so great that incident electrons may penetrate too quickly for neighboring electrons at the surface to respond. That is, the primaries may not spend enough time next to prospective secondary electrons to impart sufficient energy for them to escape. Additionally, incident electrons can penetrate so deeply that secondary electrons will not have enough energy to escape. Thus the secondary yield decreases to a value less than unity at these higher energies, and the ambient electron temperature again determines the spacecraft potential. Consistent with the high electron temperature in this region, we can expect spacecraft charging to large potentials ($> 1\ kV$). When a spacecraft is in eclipse (i.e., no photoelectrons present), the charging will be determined by the ambient ion and electron and secondary electron considerations noted here.

The energy corresponding to the $\delta(\varepsilon) = 1$ transition between regions II and III has an electron temperature associated with it. Based on the preceding discussion, above this electron temperature, the primary electron flux is greater than the secondary electron flux, and significant negative charging can occur. For a monoenergetic incident electron flow, this temperature at which $\delta(\varepsilon) = 1$ is the critical temperature.

2.2.2.4   Ambient Ions and Electrons, Photoelectrons, and Secondary Electrons.   Finally, we consider the combined influence of ambient ions and electrons, photoelectrons, and secondary and backscattered electrons. This will be the case when the spacecraft is in sunlight. On the sunlit side of the spacecraft, the photo-electron emission will dominate. While on the dark side, if $\delta(\varepsilon) < 1$, ambient ion and electron flux will determine charging, but if $\delta(\varepsilon) \geq 1$, the secondary electron emission will rule. In both cases, differential charging tends to occur even if the sunlit side swings negative since the dark side will tend to charge more negatively than the sunlit side. Once the sunlit side is charged to a few volts, a positively charged barrier potential begins to form. This barrier potential (a "saddle point" in the potential sunward of the spacecraft that causes a sunward-directed electric field between the satellite and the "minimum" of the saddle) grows as differential charging develops across the spacecraft (since one side is sunlit and the other is in darkness). Eventually, the barrier potential prevents photoelectrons from escaping the satellite, and large negative potentials can result. (Hastings & Garrett, 1996:176; private communication, D. Della-Rose, January 2003).

Recall that the charging discussion above is associated with monoenergetic ambient electrons, and this constraint will be relaxed in Section 2.6.

2.3   Charging Associated with Eclipse and Coronal Mass Ejections

DeForest (1972:655) states that a GEO spacecraft goes into eclipse for about $\frac{1}{2}$ hour every night for a period of about 3 to 4 weeks on either side of equinox. For the data examined in the present research, the duration of eclipse approached one hour by 16 March 1999. An example of this is illustrated in Figure 2 above. DeForest (1972:651) determined that ATS-5 could charge to potentials as high as 10 kV during eclipse and 200 V in sunlight.

CMEs also provide relatively large amounts of solar plasma, which is injected into the geosynchronous orbit of the spacecraft. During both eclipse charging events

and CMEs, the plasma is typically high-energy, but not necessarily dense. However, Hastings and Garrett (1996:69-70) indicate that the plasma density and high-energy portion of the distribution function increase during geomagnetic storming. This concept is consistent with the injection of magnetotail plasma into the near-Earth environment, in addition to the plasma already present. They conclude that this increase in the high-energy distribution has a decisive impact on spacecraft charging. This, too, is consistent with the higher potentials reached as the plasma density and high-energy portion of the distribution function increased as evidenced in the data examined.

The level of charging is also related to the K_p value (Garrett, 1981:580,584). Higher K_p values imply greater disturbances, which follows from higher energy plasma impinging on the near-Earth region (Kivelson and Russell, 1995:294-295). These higher particle energies can result in large spacecraft surface potentials.

2.4   Measurement of Spacecraft Potentials

A charged spacecraft attracts charged particles of the opposite sign and repels those of the same sign, resulting in an energy shift where the energies of ions and electrons inside the sheath are different from those outside the sheath. Since we consider the ambient plasma (outside the sheath) to be at zero potential, this shift represents the spacecraft potential. When hot plasma is injected into geosynchronous orbit, the hot electron flux increases, causing a satellite to charge to large negative potentials with respect to the ambient environment. This negative potential accelerates the low-energy ($\backsim 0\ eV$) ions arriving at the spacecraft, shifting ion energies by qV_{sc}. The charged spacecraft, on the other hand, repels the electrons, and this repulsion results in the electrons with energies between 0 and qV_{sc} not being measured since they don't reach the spacecraft surface (Lai, 1999:4).

If the low-energy ambient ion density is large enough, acceleration through the spacecraft sheath produces a distinct gap, or narrow peak, in the ion energy distri-

bution (i.e., an ion line) at the spacecraft potential, which can be easily identified on spectrograms or by instruments, providing a clearly identifiable measure of the potential. If no ion line is found, the spacecraft potential can be determined through iterative procedures (Garrett, 1981:580-581; Lai, 1999:3-4; Thomsen, et al., 1999:11-13). Though measurement of potentials is outside the scope of this research, the measured potentials are central to calculating corrected energies (cf. Section 3.3).

2.5   The Current Balance Equation

As previously noted, charging occurs due to an imbalance of incoming versus outgoing flux of charged particles, namely, electrons and (positive) ions. The principal particle fluxes for charging onset are those of incident electrons and secondary electrons. Strictly speaking, this is true only in eclipse, where photoelectrons are not a factor. Considering the argument in Section 2.2.2.4, we note that the barrier potential has an effect on the current balance outside of eclipse as well. Thus, differential charging effects can cause large negative charging events to commence outside of eclipse. Again, our study does not attempt to model such effects.

With regard to electron flux, the incoming electron flux is balanced by the outgoing secondary emission and backscattered electrons at the critical temperature. As noted above, we can neglect the ion flux (for charging onset) since it is approximately two orders of magnitude smaller than the electron flux.

Now consider a distribution of ambient electron energies in regions II and III (as opposed to the earlier monoenergetic assumption). While the portion of the distribution with energies corresponding to region II will result in a net flux of outgoing electrons, the part of the ambient distribution with energies in the range of region III will result in a net flux of electrons toward the spacecraft. When these two fluxes balance, the net current to the spacecraft is zero. The temperature T, where this balance occurs, is the critical temperature. But when the net electron flux toward the spacecraft (region III) exceeds the net outgoing flux (region II), the

spacecraft will charge negatively. More importantly, the spacecraft can charge to *high* negative voltages. Equation (6) gives a mathematical definition of the critical temperature.

The mathematical implementation of the Maxwellian distribution is explained in Section 2.6.1, and the implementation of the kappa distribution is in Section 3.1.

2.6   Critical Temperature

Rubin, et al., observed a threshold electron temperature below which ATS-5 instruments did not detect charging and above which charging occurred. In the spacecraft charging arena, this threshold temperature is commonly referred to the "critical temperature" for the onset of spacecraft charging. The associated spacecraft potential varied almost linearly with the electron temperature above this threshold (Rubin, et al., 1980:6, 9). Lai (1991) provides a theoretical basis for calculating the critical temperature. This threshold temperature commonly appears in the 1.5 - 2.5 *keV* range (Lai and Tautz, 2001:11), and this range is consistent for various spacecraft surface materials and configurations.

Up to now, research related to the calculation of the critical temperature has been limited to the Maxwellian approach.

2.6.1   Maxwellian Distribution.   It is appropriate to convert the velocity moment into terms of energy to obtain

$$\int_0^\infty v^3 F(v) dv = \int_0^\infty \varepsilon f(\varepsilon) d\varepsilon \tag{2}$$

where the distribution functions are appropriately normalized. Here, $F(v)$ is the velocity distribution. In the Maxwellian model, the energy distribution $f(\varepsilon)$, for a given mass m, density n, and Maxwellian temperature T_M, is

$$f_M(\varepsilon) = n \left(\frac{m}{2\pi T_M} \right)^{\frac{3}{2}} e^{\left(-\frac{\varepsilon}{T_M}\right)} \varepsilon^{\frac{1}{2}} \tag{3}$$

The secondary electron, $\delta(\varepsilon)$, and backscatter, $\eta(\varepsilon)$, coefficients are measured as functions of energy, where

$$\delta(\varepsilon) = c(e^{-\frac{\varepsilon}{a}} - e^{-\frac{\varepsilon}{b}}) \tag{4}$$

and

$$\eta(\varepsilon) = A - Be^{-\varepsilon C} \tag{5}$$

as determined (by data fits) by Sanders and Inouye (1978:74) and Prokopenko and Laframboise (1980:4127), respectively. Here $a = 4.3E_{max}$, $b = 0.367E_{max}$ and $c = 1.37\delta_{max}$. δ_{max} is the maximum value of $\delta(\varepsilon)$, and E_{max} is the primary electron energy corresponding to δ_{max} (Lai, 1991:1630). Prokopenko and Laframboise (1980:4127) state, "The coefficients A, B, and C are functions of the atomic number Z of the surface material." To emphasize, these values are material dependent. It is convenient to calculate the current balance in terms of energy (cf. Lai, 1991:1630). When the incident electron flux is balanced by the secondary and backscattered flux, the spacecraft potential is zero, and we can write the current balance equation as

$$\int_0^\infty \varepsilon^{\frac{1}{2}} f(\varepsilon) d\varepsilon = \int_0^\infty \varepsilon^{\frac{1}{2}} f(\varepsilon)[\delta(\varepsilon) + \eta(\varepsilon)] d\varepsilon \tag{6}$$

$$\int_0^\infty \varepsilon e^{\left(-\frac{\varepsilon}{T_M}\right)} d\varepsilon = \int_0^\infty \varepsilon e^{\left(-\frac{\varepsilon}{T_M}\right)}[c(e^{-\frac{\varepsilon}{a}} - e^{-\frac{\varepsilon}{b}}) + A - Be^{-\varepsilon C}] d\varepsilon \tag{7}$$

where Equation (6) is valid for an arbitrary energy distribution function, and Equation (7) follows when the distribution function in Equation (3) is substituted into Equation (6). Observe that the normalization constants divide out since $f_M(\varepsilon)$ is

a term on both sides of the equation, so there is no dependence on electron density (Lai, 1991:1630). Recall that ion flux is omitted since it is not substantial when considering spacecraft charging *onset*. Integrating Equation (6) and simplifying yields

$$c[(1 + \frac{T_M}{a})^{-2} + (1 + \frac{T_M}{b})^{-2}] + A - B(1 + T_M C)^{-2} - 1 = 0 \tag{8}$$

The solution T_M of this equation is the critical temperature for charging onset, assuming a Maxwellian plasma. Strictly speaking, this equation is valid for spacecraft in eclipse since photoelectrons are not considered. Note that the resulting critical temperature is material dependent. For example, the critical temperature is 1.341 keV for non-activated CuBe, and 0.5 keV for kapton. Both of these materials are examined in the present research. Lai and Della-Rose (2001:923) present a table of critical temperatures (rounded up to the next 0.1 keV) for various materials.

2.6.2   The Need for a Non-Maxwellian Distribution.   For relatively low-energy particles ($\sim 10\ keV$ or less) in space, the Maxwell distribution gives accurate results for electron and ion velocity distributions (Meyer-Vernet, 2001:248). We expect the Maxwell distribution to be representative since lower thermal energies (particle velocities) result in larger collision cross-sections. Conversely, as velocities increase, cross-sections decrease. Thus it follows that the collisional properties of a gas would become less dominant.

Therefore, the weakness of the Maxwell distribution for space plasmas at or near geosynchronous satellite orbits is attributable to the fact that the thermal energy (velocity) is high while the density is often low. Thus the mean free path of particles sometimes becomes greater than the scale height, which is the length-scale corresponding to a $1/e$ (exponential) decrease in plasma density and pressure with altitude, resulting in an essentially collisionless plasma. So the non-equilibrium processes limit the practical application of the Maxwell distribution to this problem (Meyer-Vernet, 1999:173). Specifically, the lack of collisions leads to a high-energy

19

tail not captured by the Maxwellian distribution. This leads to the need for a non-Maxwellian distribution to describe the environment at high energies ($> 10 \ keV$).

As early as the mid-1960s, observations from electrostatic analyzers flown aboard Soviet spacecraft showed that plasma sheet electrons exhibit a quasi-thermal energy spectrum and a high-energy non-Maxwellian tail (Vasyliunas, 1968:2841). The plasma sheet is a sheet-like current on the night side of the magnetosphere (Parks, 1991:61), and the "inner boundary of the plasma sheet varies from about 5.5 to 12 R_E." (Vasyliunas, 1968:2849). To illustrate, consider that if the temperature is chosen such that the lower energy channels of the analyzers are well represented, then the higher energy channels are excluded from the fit, suggesting evidence of a high-energy, non-Maxwellian tail (Vasyliunas, 1968:2866). It will be shown that this high-energy tail is primarily responsible for spacecraft charging.

2.6.3 The Suitability of the kappa Distribution. One approach that allows for an essentially collisionless medium and captures the high-energy tail (Christon, et. al., 1988:2562) is utilizing the kappa distribution. The kappa distribution is especially suitable since the limiting case (as kappa approaches infinity) converges to the Maxwellian distribution. The superiority of the kappa distribution over the Maxwellian as fitted to data from three environments – namely, near-Earth, near-Jupiter, and near-Saturn, has been demonstrated for this problem with regard to particle velocities and fluxes (Meyer-Vernet, 2001:247-248).

Figure 4, after Meyer-Vernet (1999:174), depicts the high-energy tail for $\kappa = 3$ and $\kappa = 6$ against a normalized velocity distribution, as in Equation (9). The Maxwellian distribution, which corresponds to $\kappa = \infty$ (see Equation (10), for example) is also plotted. Notice the similarity in the distributions for $v \leq w$, whereas the kappa distributions have an excess of high-speed particles not captured by the Maxwellian distribution. The distributions are normalized so they have the same number density and same most probable speed. Therefore, the low-energy distri-

bution differences between the Maxwellian and kappa distribution functions are minimized. But the excess of high-energy particles in the kappa distributions, as compared to the Maxwellian, is compensated by the lack of low-energy particles. (Meyer-Vernet, 1999:174 and 2001:249; personal correspondence, D. Della-Rose, March 2003).
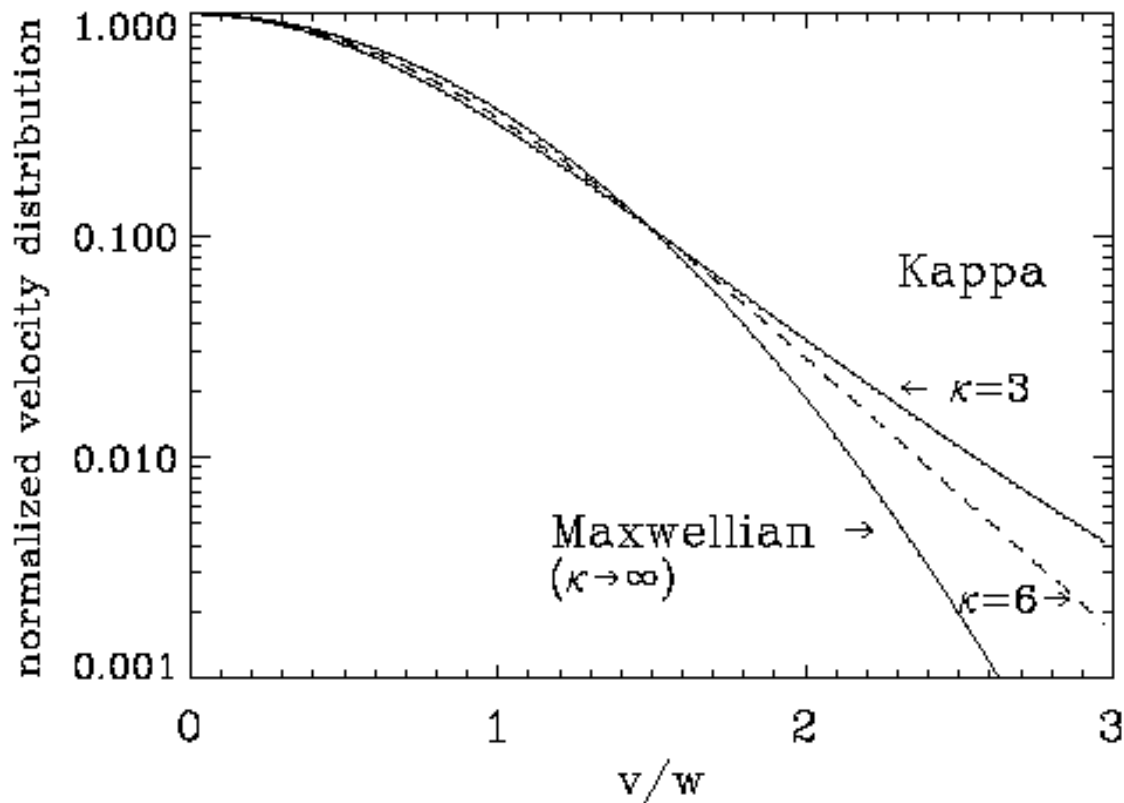
Figure 4   kappa velocity distributions (Equation (9)) for $\kappa = 3$ (solid line) and $\kappa = 6$ (dashed line), respectively, plotted versus the speed normalized to the most probable speed. The limiting case $\kappa \to \infty$, which is simply the Maxwell distribution $exp(-v^2/w^2)$, and which has the same most probable speed is superimposed.

Figure 5, plotted using the kappa velocity distribution function in Equation (9), illustrates the difference between a Maxwellian distribution and a kappa distribution

for capturing the high-energy tail of the distribution function determined using the LANL data. The data are taken from LANL 1991-080 at 22.04 UT (22.57 LT) on 14 March 1999, with a measured spacecraft potential of $-2.51\ kV$. The kappa distribution is calculated with $\kappa = 3.5$, and the Maxwellian is, equivalently, $\kappa = \infty$. The kappa temperature is $T_\kappa = 5.59\ keV$. The Maxwellian temperature, derived from the relationship in Equation (31) and based on the best fit value of kappa, is $T_M = 3.20\ keV$. As explained in Section 3.3, this is the temperature of a Maxwellian distribution possessing the same most probable speed as the kappa distribution.

All data fits were plotted using the kappa velocity distribution function in Equation 9. Emphasis was placed on fitting the kappa and Maxwellian distribution functions to the high-energy portion of the measured distribution functions, since this high-energy component is responsible for significant charging. The low-energy portions of the particle (electron) distributions are thought to be either photoelectrons or trapped secondaries – i.e., secondary electrons that cannot escape the barrier potential (private communication among V. Davis, S. Lai, and D. Della-Rose, December 2002).

Also, observe the energy shift as explained in Section 2.4. This energy shift is responsible for the fact that no electron data are observed for energies less that 2.51 keV (the energy corresponding to the spacecraft potential). Finally, it is clear that the high-energy tail is readily captured by the kappa distribution, but not by the Maxwellian.
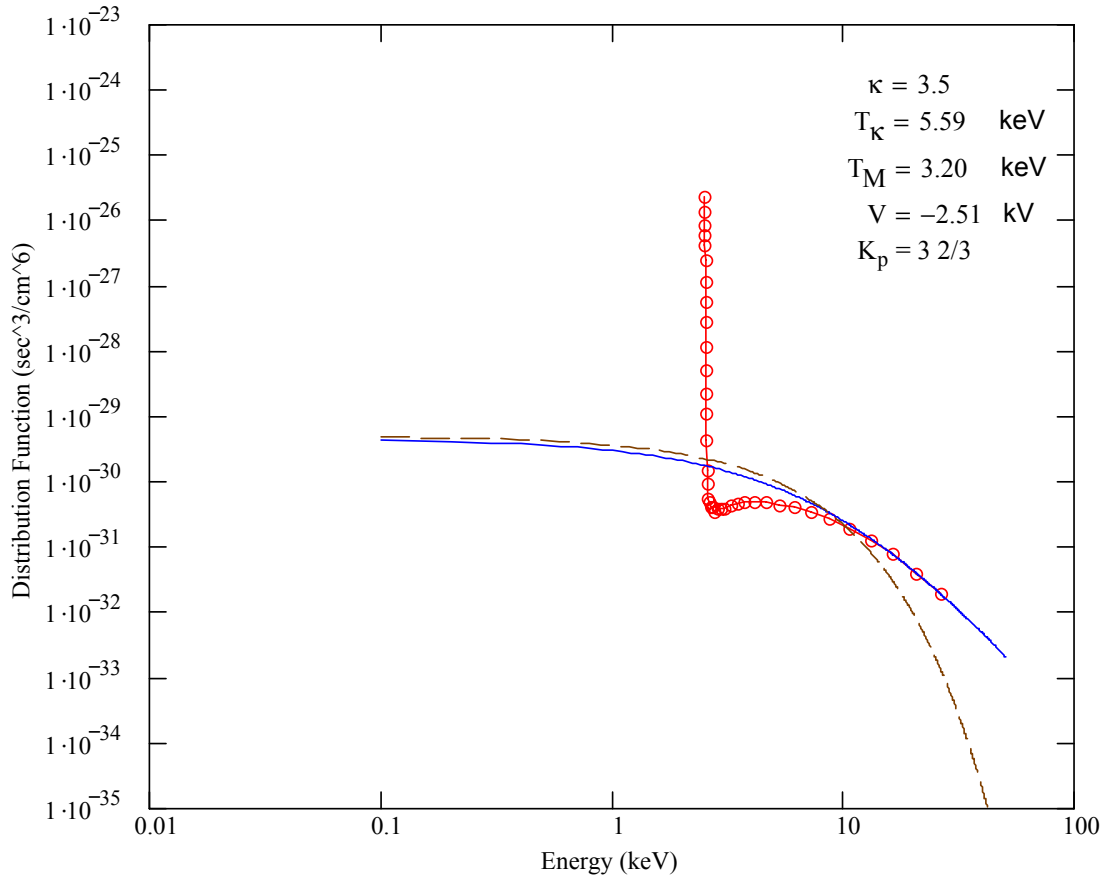
Figure 5   Electron Distribution Function vs. Electron Energy for LANL 1991-080
Data at 22.04 UT (22.57 LT) on 14 March 1999 Demonstrating Superior-
ity of the kappa Distribution over the Maxwellian at Capturing the High
Energy Tail. Plotted are LANL Data Values (circles), kappa Distribution
(solid), and Maxwellian Distribution (dash). (Data Courtesy of Michelle
F. Thomsen, Los Alamos National Laboratory.)

Vasyliunas was possibly the first to use the kappa distribution in its general
form and to note its relationship to the Maxwellian. He presents the kappa velocity
distribution as (Vasyliunas, 1968:2866-2867)

$$f_\kappa(v) = \frac{n}{\left(\kappa w_0^2\right)^{\frac{3}{2}}} \frac{\Gamma\left(\kappa + 1\right)}{\pi^{\frac{3}{2}} \Gamma\left(\kappa - \frac{1}{2}\right)} \left[1 + \frac{v^2}{\kappa w_0^2}\right]^{-(\kappa+1)} \tag{9}$$

where

$$n \;\;= \text{the total number density}$$

$$w_0 = \text{the most probable speed}$$

$$\kappa \;\;= \text{the exponent of the differential flux at high energies}$$

That is, κ is really only of consequence in the high-energy portion of the distribution, since this part of the distribution is the basis for *significant* charging. Vasyliunas notes appearances of kappa distributions, specifically with $\kappa = 2$, in earlier literature (Vasyliunas, 1968:2866-2867; Summers and Thorne, 1991:1836). It is the inverse power law relation

$$f_\kappa(v) \propto \left[1 + \frac{v^2}{\kappa w_0^2}\right]^{-(\kappa+1)}$$

that is crucial to capturing the high-energy tail missed by the Maxwellian (Vasyliunas, 1968:2866; Meyer-Vernet, 2001:248-249). Larger kappa values are more like the Maxwellian, but the high-energy tail is captured by lower kappa values (Summers and Thorne, 1991:1836). Here we also note that

$$\lim_{\kappa \to \infty} \left[1 + \frac{v^2}{\kappa w_0^2}\right]^{-(\kappa+1)} \;=\; e^{-\frac{mv^2}{2T_M}}$$
$$\;=\; f_M(v) \tag{10}$$

which is the Maxwellian velocity distribution.

III. Approach

The approach taken for this research, which was geared toward suggestions by Dr. Shu T. Lai of the Air Force Research Laboratory (personal correspondence between S. Lai and D. Della-Rose, November 2001) was to first become familiar with the Maxwellian theory which is presented in Section 2.6.1. This included a study of the distribution function and the current balance equation using secondary and backscattered coefficients. The next step was to become familiar with kappa theory and understand its application to the high-energy tail in the electron distribution functions. This was followed by formulation of the kappa current balance equation with secondary and backscattered coefficients and deriving the analytical result. Finally, comparison was made with the analytical results and observations.

3.1   Development of the Current Balance Equation Using the kappa Distribution

As in the Maxwellian model, we can define the kappa energy distribution function for a given mass m, density n, and (kappa) temperature T_κ (in energy units), as

$$
\begin{aligned}
f_\kappa(\varepsilon) &= n A_\kappa \left(\frac{2}{\kappa m w^2} \right)^{\frac{3}{2}} \varepsilon^{\frac{1}{2}} \left[1 + \frac{\varepsilon}{\left(\kappa - \frac{3}{2} \right) T_\kappa} \right]^{-(\kappa+1)} \quad &(11) \\
&= n A_\kappa \left[\left(\kappa - \frac{3}{2} \right) T_\kappa \right]^{-\frac{3}{2}} \varepsilon^{\frac{1}{2}} \left[1 + \frac{\varepsilon}{\left(\kappa - \frac{3}{2} \right) T_\kappa} \right]^{-(\kappa+1)} \quad &(12)
\end{aligned}
$$

where we note the requirement that $\kappa > 3/2$ and A_κ is the normalization factor

$$
A_\kappa = \frac{\Gamma(\kappa + 1)}{\Gamma(\frac{3}{2})\Gamma(\kappa - \frac{1}{2})} \tag{13}
$$

So the integral form of the current balance equation (with normalization terms cancelled since they are not functions of ε) is then

$$\int_0^\infty \varepsilon \left[1 + \frac{\varepsilon}{\left(\kappa - \frac{3}{2}\right)T_\kappa}\right]^{-(\kappa+1)} d\varepsilon$$

$$= \int_0^\infty \varepsilon \left[1 + \frac{\varepsilon}{\left(\kappa - \frac{3}{2}\right)T_\kappa}\right]^{-(\kappa+1)} [c(e^{-\frac{\varepsilon}{a}} - e^{-\frac{\varepsilon}{b}}) + A - Be^{-\varepsilon C}]d\varepsilon \qquad (14)$$

Recall that this is an integration of the velocity moment as in Equation (2).

Originally, the integration was carried out in MATLAB$^{\circledR}$, which returned the left-hand side of the equation as

$$\int_0^\infty \varepsilon \left[1 + \frac{\varepsilon}{\left(\kappa - \frac{3}{2}\right)T_\kappa}\right]^{-(\kappa+1)} d\varepsilon = \left[\frac{(2\kappa - 3)T_\kappa}{2(\kappa - 1)}\right]^2 \qquad (15)$$

but not in this simplified form, and MATLAB$^{\circledR}$ returned the right-hand side as

$$\int_0^\infty \varepsilon \left[1 + \frac{\varepsilon}{\left(\kappa - \frac{3}{2}\right)T_\kappa}\right]^{-(\kappa+1)} [c(e^{-\frac{\varepsilon}{a}} - e^{-\frac{\varepsilon}{b}}) + A - Be^{-\varepsilon C}]d\varepsilon$$

$$= \frac{(2\kappa - 3)T_\kappa}{2\Gamma(\kappa + 1)}ca\{\Gamma(\kappa - 1)\frac{(2\kappa - 3)T_\kappa}{2a}M\left(2, 2 - \kappa, \frac{(2\kappa - 3)T_\kappa}{2a}\right)$$

$$+ \pi\csc(\pi\kappa)\kappa\left[\frac{(2\kappa - 3)T_\kappa}{2a}\right]^\kappa M\left(\kappa + 1, \kappa, \frac{(2\kappa - 3)T_\kappa}{2a}\right)\}$$

$$- \frac{(2\kappa - 3)T_\kappa}{2\Gamma(\kappa + 1)}cb\{\Gamma(\kappa - 1)\frac{(2\kappa - 3)T_\kappa}{2b}M\left(2, 2 - \kappa, \frac{(2\kappa - 3)T_\kappa}{2b}\right)$$

$$+ \pi\csc(\pi\kappa)\kappa\left[\frac{(2\kappa - 3)T_\kappa}{2b}\right]^\kappa M\left(\kappa + 1, \kappa, \frac{(2\kappa - 3)T_\kappa}{2b}\right)\}$$

$$+ \left[\frac{(2\kappa - 3)T_\kappa}{2(\kappa - 1)}\right]^2 A$$

$$- \frac{(2\kappa - 3)T_\kappa B}{2\Gamma(\kappa + 1)C}\{\Gamma(\kappa - 1)\frac{(2\kappa - 3)T_\kappa C}{2}M\left(2, 2 - \kappa, \frac{(2\kappa - 3)T_\kappa C}{2}\right)$$

$$+ \pi\csc(\pi\kappa)\kappa\left[\frac{(2\kappa - 3)T_\kappa C}{2}\right]^\kappa M\left(\kappa + 1, \kappa, \frac{(2\kappa - 3)T_\kappa C}{2}\right)\} \qquad (16)$$

which is likewise simplified from the original MATLAB® result for display here.

Dividing through by the left-hand side of Equation (14) and further simplifying yields

$$
\begin{aligned}
& c\{M\left(2, 2-\kappa, \frac{(2\kappa-3)T_\kappa}{2a}\right) \\
& +\frac{\pi\kappa\csc(\pi\kappa)}{\Gamma(\kappa-1)}\left[\frac{(2\kappa-3)T_\kappa}{2a}\right]^{\kappa-1} M\left(\kappa+1, \kappa, \frac{(2\kappa-3)T_\kappa}{2a}\right) \\
& -M\left(2, 2-\kappa, \frac{(2\kappa-3)T_\kappa}{2b}\right) \\
& +\frac{\pi\kappa\csc(\pi\kappa)}{\Gamma(\kappa-1)}\left[\frac{(2\kappa-3)T_\kappa}{2b}\right]^{\kappa-1} M\left(\kappa+1, \kappa, \frac{(2\kappa-3)T_\kappa}{2b}\right)\} \\
& -B\{M\left(2, 2-\kappa, \frac{(2\kappa-3)T_\kappa C}{2}\right) \\
& +\frac{\pi\kappa\csc(\pi\kappa)}{\Gamma(\kappa-1)}\left[\frac{(2\kappa-3)T_\kappa C}{2}\right]^{\kappa-1} M\left(\kappa+1, \kappa, \frac{(2\kappa-3)T_\kappa C}{2}\right)\} \\
& +A-1 \\
= \ & 0
\end{aligned}
\tag{17}
$$

Now observe that

$$
\begin{aligned}
\frac{\pi\kappa\csc(\pi\kappa)}{\Gamma(\kappa-1)} &= \frac{\kappa(-\kappa)\Gamma(-\kappa)\Gamma(\kappa)}{\Gamma(\kappa-1)} \\
&= -\frac{\Gamma(\kappa+1)\Gamma(2-\kappa)}{(\kappa-1)\Gamma(\kappa-1)} \\
&= -\frac{\Gamma(\kappa+1)\Gamma(2-\kappa)}{\Gamma(2)\Gamma(\kappa)}
\end{aligned}
\tag{18}
$$

since (Abramowitz and Stegun, 1965:256)

$$
\pi\csc(\pi\kappa) = (-\kappa)\Gamma(-\kappa)\Gamma(\kappa)
$$

27

and

$$\Gamma(2) = 1$$

Now we note that

$$
\frac{\kappa}{\Gamma(\kappa - 1)} = -\frac{\Gamma(\kappa + 1)\Gamma(2 - \kappa)}{\Gamma(2)\Gamma(\kappa)}\frac{\sin \pi\kappa}{\pi} \tag{19}
$$

$$
= -\frac{\Gamma(\kappa + 1)\Gamma(2 - \kappa)}{\Gamma(2)\Gamma(\kappa)}\frac{1}{\Gamma(\kappa)\Gamma(1 - \kappa)} \tag{20}
$$

and consider

$$
M(2, 2 - \kappa, z) + \frac{\pi\kappa \csc(\pi\kappa)}{\Gamma(\kappa - 1)} z^{\kappa - 1} M(\kappa + 1, \kappa, z)
$$

$$
= M(2, 2 - \kappa, z) + \frac{\kappa}{\Gamma(\kappa - 1)}\frac{\pi}{\sin \pi\kappa} z^{\kappa - 1} M(\kappa + 1, \kappa, z)
$$

$$
= z^{\kappa - 1}\frac{\pi}{\sin \pi\kappa}\left\{ z^{1-\kappa}\frac{M(2, 2 - \kappa, z)}{\pi \csc(\pi\kappa)} + \frac{\kappa}{\Gamma(\kappa - 1)} M(\kappa + 1, \kappa, z)\right\}
$$

$$
= z^{\kappa - 1}\frac{\pi}{\sin \pi\kappa}\left\{ z^{1-\kappa}\frac{M(2, 2 - \kappa, z)}{\Gamma(\kappa)\Gamma(1 - \kappa)} - \frac{\Gamma(\kappa + 1)\Gamma(2 - \kappa)}{\Gamma(2)\Gamma(\kappa)}\frac{M(\kappa + 1, \kappa, z)}{\Gamma(\kappa)\Gamma(1 - \kappa)}\right\}
$$

$$
= z^{\kappa - 1}\kappa(\kappa - 1)\frac{\pi}{\sin \pi\kappa}\left\{ \frac{M(\kappa + 1, \kappa, z)}{\Gamma(2)\Gamma(\kappa)} - z^{1-\kappa}\frac{M(2, 2 - \kappa, z)}{\Gamma(\kappa + 1)\Gamma(2 - \kappa)}\right\} \tag{21}
$$

$$
= z^{\kappa - 1}\kappa(\kappa - 1)\frac{\pi}{\sin \pi b}\left\{ \frac{M(a, b, z)}{\Gamma(1 + a - b)\Gamma(b)} - z^{1-b}\frac{M(1 + a - b, 2 - b, z)}{\Gamma(a)\Gamma(2 - b)}\right\}
$$

$$
= z^{\kappa - 1}\kappa(\kappa - 1) U(a, b, z) \tag{22}
$$

where we let $a = \kappa + 1$ and $b = \kappa$, corresponding to the definition of Kummer's function (Abramowitz and Stegun, 1965:504),

$$
M(a, b, z) = 1 + \frac{az}{b} + \frac{(a)_2 z^2}{(b)_2 2!} + \cdots + \frac{(a)_n z^n}{(b)_n n!} + \cdots
$$

where

$$(a)_n = a(a+1)(a+2)\dots(a+n-1)$$

$$(a)_0 = 1$$

and

$$U(a,b,z) = \frac{\pi}{\sin \pi b}\left[\frac{M(a,b,z)}{\Gamma(1+a-b)\Gamma(b)} - z^{1-b}\frac{M(1+a-b,2-b,z)}{\Gamma(a)\Gamma(2-b)}\right]$$

This leads to our initial result for the kappa current balance equation:

$$\kappa(\kappa-1)\left[\frac{(2\kappa-3)T_\kappa}{2}\right]^{\kappa-1}\{ca^{1-\kappa}U\left(\kappa+1,\kappa,\frac{(2\kappa-3)T_\kappa}{2a}\right)$$

$$-cb^{1-\kappa}U\left(\kappa+1,\kappa,\frac{(2\kappa-3)T_\kappa}{2b}\right) - BC^{\kappa-1}U\left(\kappa+1,\kappa,\frac{(2\kappa-3)T_\kappa C}{2}\right)\}$$

$$+A-1$$

$$= 0 \tag{23}$$

The solution T_κ of this equation is the critical (kappa) temperature for charging onset for a given material and value of kappa. For reference, a table of critical temperatures calculated for non-activated CuBe over a range of values, $\kappa = 2.5$ to 17.5, is available in Appendix D.

However, a more direct approach is the Whittaker function (Appendix B). The practical application of the Whittaker function came to light long after the initial analysis of the current balance equation was complete. The graphs of the two are (theoretically) identical, but the Whittaker function converges more quickly to the Maxwellian possibly since there is less error propagation due to round-off in the numerical calculations.

Graphical results of the kappa current balance equation (Eq. (23)) compared to the Maxwellian (Eq. (8)) are displayed in Figure 6, which is a graph of the left-hand side of the current balance equation. It can serve as a graphical method of finding the roots of the current balance equation. However, the only useful pieces of information obtained from this graph are the roots, which define threshold energies related to charging. Observe how quickly the kappa distribution curves approach the Maxwellian with increasing value of kappa from 1.6 to 2.5 and then 5.5. Notice also that the apparent difference slows from $\kappa = 2.5$ to $\kappa = 5.5$ as compared to that from $\kappa = 1.6$ to $\kappa = 2.5$. In Figure 6, the kappa current balance equation is displayed using the Whittaker function form.
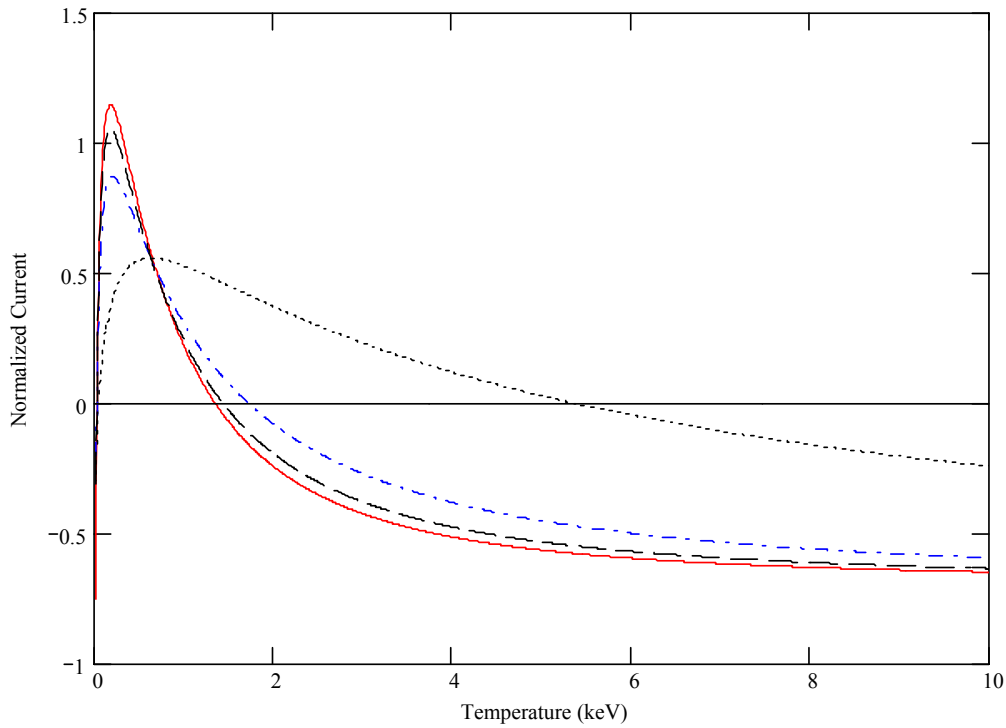
Figure 6   Normalized Current I/I_0 vs. Electron Temperature for non-activated CuBe. Curves are the kappa Current Balance Equation with $\kappa = 1.6$ (dot), $\kappa = 2.5$ (dash-dot), $\kappa = 5.5$ (dash), and the Maxwellian Current Balance Equation (solid).

If, as is sometimes the case, $C = 0$, then we can represent the backscattered coefficient term in the current balance equation by B. This is necessary since

$$\lim_{z \to 0} U(a, b, z) \to z^{-a} \tag{24}$$

and when $C = 0$, $z = 0$, and we have a singularity. In such a case, since $\kappa > 3/2$, we can also make use of the fact that the rates of convergence for C'^{k-1} and $U(a, b, 0)$ are the same. That is, for $C = 0$,

$$\lim_{C \to 0} C'^{\kappa-1} U\left(\kappa + 1, \kappa, \left(\kappa - \frac{3}{2}\right) T_\kappa C\right) = \lim_{C \to 0} C'^{\kappa-1} U(\kappa + 1, \kappa, 0)$$
$$= 1$$

$$C = 0 \Longrightarrow C'^{\kappa-1} \frac{M(a, b, z)}{\Gamma(1 + a - b)\Gamma(b)} = 0$$

and

$$\lim_{z \to 0} C'^{\kappa-1} z^{1-\kappa} \frac{M(1 + a - b, 2 - b, 0)}{\Gamma(a)\Gamma(2 - b)} = \frac{1}{\Gamma(a)\Gamma(2 - b)}$$
$$= \frac{1}{\Gamma(\kappa + 1)\Gamma(2 - \kappa)}$$
$$= \frac{1}{\pi \csc[\pi(2 - \kappa)]}$$

which yields

$$
\begin{aligned}
& C'^{\kappa-1} U(\kappa + 1, \kappa, 0) \\
&= \frac{\pi}{\sin[\pi(2 - \kappa)]} \left[C'^{\kappa-1} \frac{M(a, b, 0)}{\Gamma(1 + a - b)\Gamma(b)} - C'^{\kappa-1} z^{1-b} \frac{M(1 + a - b, 2 - b, 0)}{\Gamma(a)\Gamma(2 - b)} \right] \\
&= \frac{\pi}{\sin[\pi(2 - \kappa)]} \left[0 - 1 \frac{1}{\pi \csc[\pi(2 - \kappa)]} \right] \\
&= -1
\end{aligned}
$$

and the last term in the current balance equation takes on the value of B (private communication, Aihua W. Wood, December 2002). As in the case of the Kummer form of the current balance equation, we can set the backscattered coefficient term in the Whittaker form to B when $C = 0$. Figure 7 is a graph of the normalized current vs. temperature for kapton – a material for which $C = 0$.
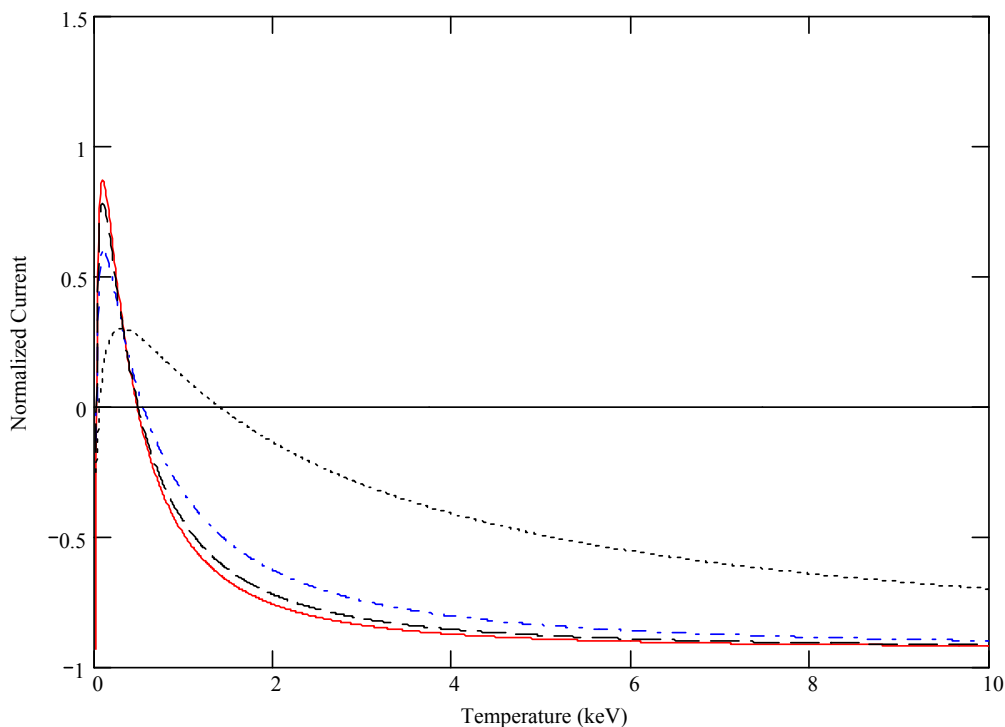
Figure 7   Normalized Current I/I_0 vs. Electron Temperature for kapton. Curves are the kappa Current Balance Equation with $\kappa = 1.6$ (dot), $\kappa = 2.5$ (dash-dot), $\kappa = 5.5$ (dash), and the Maxwellian Current Balance Equation (solid).

3.2   Data Selection and Acquisition

Following the determination of the dates of interest for comparison to data analyzed by Lai and Della-Rose (2001), the data were made available for ftp acquisition by the Los Alamos National Laboratory. The data were then converted into

a useable format for graphical analysis in Mathcad®. However, the LANL data obtained covered only a subset of the cases examined in Lai and Della-Rose (2001), so emphasis was placed on eclipse charging events occurring in March 1999. Data for April 1999, and June 2000 were also examined for significant (potential $> 1 \ kV$) spacecraft charging events.

Data measurements were taken by magnetospheric plasma analyzers (MPAs) deployed on a number of Department of Energy GEO satellites. The purpose of the MPAs is to monitor the three-dimensional plasma electron and ion distributions at GEO in support of the spacecraft mission (Thomsen, et al., 1999:1). The data studied were angle-averaged from the full three-dimensional distribution, which is obtained in one approximately 10-second satellite spin (Thomsen, et al., 1999:1).

The charging events selected include the following associated data used in this study:

Date-time group (UT and spacecraft LT), spacecraft geographic coordinates (km - discussed in Appendix A), spacecraft potential (V), IP flags, electron density ($\#/cm^{-3}$), parallel and perpendicular hot electron temperatures, and differential particle fluxes in each of 40 channels. IP flags signify whether an ion line was found or an iteration procedure was used to determine the spacecraft potential. The use of ion lines to determine spacecraft potential is generally considered reliable (Thomsen, et al., 1999:11-13). Based on a graphical comparison of data for ion lines found vs. iteration, iteration data also appeared reliable.

The particle fluxes in the data were measured at the instrument, but were not corrected for spacecraft potential (personal correspondence between M. Thomsen and D. Della-Rose, October 2002). The temperatures are experimentally derived using

$$T = \frac{1}{n}\int m\left(\mathbf{v}-\mathbf{V}\right)\left(\mathbf{v}-\mathbf{V}\right)f(\mathbf{v})d^3\mathbf{v} \tag{25}$$

$$= \frac{1}{n}\int m\left(\mathbf{vv}\right)f(\mathbf{v})d^3\mathbf{v}-m\mathbf{VV} \tag{26}$$

where $\mathbf{v}$ is the total velocity, $\mathbf{V}$ is the average velocity of the electrons in the plasma, and $f(\mathbf{v})$ is the measured phase space density as a function of $\mathbf{v}$. The distribution function based on channel energy data is determined by multiplying the differential flux F ($cm^{-2}\ s^{-1}\ sr^{-1}\ eV^{-1}$) by K_e and dividing this product by the center energy E_c (eV) for that channel (Thomsen, et al., 1999:2, 14-15, 18-19). That is,

$$f_{data_i} = \frac{F_i K_e}{E_{c_i}} \tag{27}$$

where i is the channel number (1-40) and

$$K_e = \frac{m_e^2}{2} = 1.616 \times 10^{-31} eV^2 cm^{-4} s^4 \tag{28}$$

3.3   Method of Analysis

Three distribution functions were plotted against the channel center energies on a log-log plot and *visually* analyzed. The distribution functions examined were from the LANL data, the kappa distribution, and the Maxwellian distribution. Visual fitting was utilized because the numerical routines for fitting failed to achieve reasonable results. Though the distribution functions averaged out in the numerical routines, the averages resulted from large deviations above and below the measured distributions (i.e., the fits were clearly poor).

All data fits were plotted using the kappa velocity distribution function in Equation (9). Emphasis was placed on fitting the kappa and Maxwellian distribution functions to the high-energy portion of the measured distribution functions, since

this high-energy component is responsible for significant charging. The low-energy portions of the particle (electron) distributions are thought to be either photoelectrons or trapped secondaries (i.e., secondary electrons that cannot escape the barrier potential), as opposed to being part of the ambient plasma.

The channel center energies are calculated by taking the geometric mean of the (corrected) edge energies E_d for each channel. The corrected energy of a particle (based on the energy shift as explained in Section 2.4) can be represented by taking the energy at infinity E' and subtracting the spacecraft potential, i.e., (Thomsen, et al., 1999:14)

$$E = E' - qV_{sc} \tag{29}$$

The distribution function graphs were then examined to *visually fit* a kappa value to the high-energy, non-Maxwellian tails of the plots. Observe that on the log-log plots, since

$$\log \left[1 + \frac{\varepsilon}{\left(\kappa - \frac{3}{2}\right)T_\kappa}\right]^{-(\kappa+1)} = -(\kappa+1)\log\left[1 + \frac{\varepsilon}{\left(\kappa - \frac{3}{2}\right)T_\kappa}\right] \tag{30}$$

the kappa values determined the slopes of the curves when the second term in the argument of the logarithm is much greater than 1. Next, the kappa temperature was varied until a fit was achieved. This kappa temperature was converted to a Maxwellian representation by using the temperature conversion

$$T_M = \frac{\left(\kappa - \frac{3}{2}\right)}{\kappa}T_\kappa \tag{31}$$

where T_κ is derived by computing $\frac{1}{2}m\left\langle v^2 \right\rangle$ (i.e., the average kinetic energy) for the kappa distribution and equating it to $\frac{3}{2}T_\kappa$. The relationship between T_M and T_κ follows from the fact that the most probable speed, w_0, is independent of kappa

and from the relationship in Equation (10) (personal communication, D. Della-Rose, February 2003). Notice that

$$\lim_{\kappa \to \infty} \frac{\kappa - \frac{3}{2}}{\kappa} T_\kappa = T_M \tag{32}$$

The Maxwellian temperature was then input into a Maxwellian distribution and plotted.

In addition to a visual inspection for curve fitting, electron number densities for the range of channels that correlated to a good visual fit were computed. The number densities for the data were used as a basis for comparison. This technique aided in refining the fit by eliminating some of the subjectivity, especially when a range of temperatures seemed to provide a good kappa fit. The temperature that returned the nearest kappa distribution number density compared to the measured data number density was used. The equations for data number density, kappa number density and Maxwellian number density were, respectively,

$$n_{data} = 4\pi \left(\frac{2}{m_e}\right)^{\frac{3}{2}} \sum_{k=low}^{high} E_{c_k} \left(\sqrt{E_{d_{k-1}} + qV_{sc}} - \sqrt{E_{d_k} + qV_{sc}}\right) f_{data_k} \tag{33}$$

$$n_\kappa \left(\kappa, T_\kappa\right) = 2n_{he} A_\kappa \left[\left(\kappa - \frac{3}{2}\right) T_\kappa\right]^{-\frac{3}{2}}$$
$$\sum_{k=low}^{high} E_{c_k} \left(\sqrt{E_{d_{k-1}} + qV_{sc}} - \sqrt{E_{d_k} + qV_{sc}}\right) \left[1 + \frac{E_{c_k}}{\left(\kappa - \frac{3}{2}\right) T_\kappa}\right]^{-(\kappa+1)} \tag{34}$$

$$n_M(T_M) = 4\pi \left(\frac{1}{\pi T_M}\right)^{\frac{3}{2}} n_{he} \sum_{k=low}^{high} E_{c_k} \left(\sqrt{E_{d_{k-1}} + qV_{sc}} - \sqrt{E_{d_k} + qV_{sc}}\right) e^{\left(-\frac{E_{c_k}}{T_M}\right)}$$

$$(35)$$

where *low* is the lowest channel number (corresponding to highest energy channel), and *high* is the highest channel number fitted, q is the charge on the particle of interest (electron), and E_c and E_d are the corrected channel center energy and uncorrected channel edge energy, respectively. For example, consider Figure 8 where channels 1-7 are fit well with the kappa curve. Note, too, that n_κ and n_M are functions of n_{he}, the hot electron number density provided in the LANL data. A partial table of (uncorrected) channel energies is available in Appendix C.

Figures 8 and 9 show the electron distribution function vs. electron energy for 09 March 1999 at 16.67 UT (23.57 LT) and 16.79 UT (23.69 LT), respectively, for LANL 1994-084 data. The time in Figure 8 is about 8 minutes before the satellite enters eclipse and near the onset of a period of charging. In this figure, $\kappa = 5.5$, the kappa temperature from the fitting procedure is $T_\kappa = 1.43 \; keV$, the Maxwellian temperature is $T_M = 1.04 \; keV$, and the spacecraft potential is $V = -22 \; V$. The geomagnetic index was $K_p = 3\frac{1}{3}$ during this time frame.

Figure 8   Electron Distribution Function vs. Electron Energy for LANL 1994-084
Data taken at 16.67 UT (23.57 LT) on 09 March 1999. Plotted are LANL
data values (circles), kappa distribution (solid line), and Maxwellian Dis-
tribution (dash). (Data Courtesy of Michelle F. Thomsen, Los Alamos
National Laboratory.)

Figure 9 is during eclipse and clearly shows the effect of the energy shift where
the electron energies that are lower than required to reach the spacecraft are cut
off. We shall denote the region where the low-energy electrons are cut off (due to
the high satellite potential) as the *forbidden* region. Here, $\kappa = 4.5$, $T_\kappa = 3.15$
keV, the Maxwellian temperature is $T_M = 2.10\ keV$, and the spacecraft potential is
$-2.14\ kV$. For the cases examined, where eclipse charging was significant ($> 1\ kV$),

charging normally began as eclipse approached, and the potential tended to reach the maximum values for the day during eclipse.
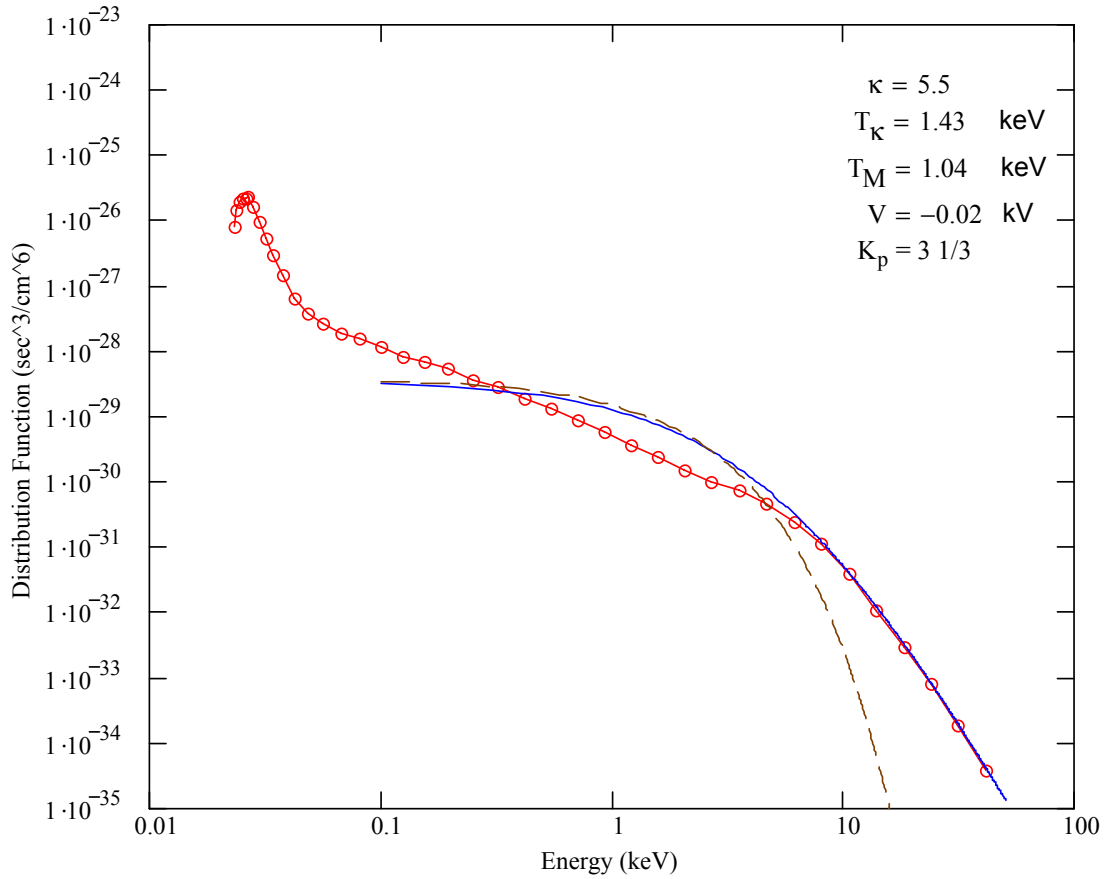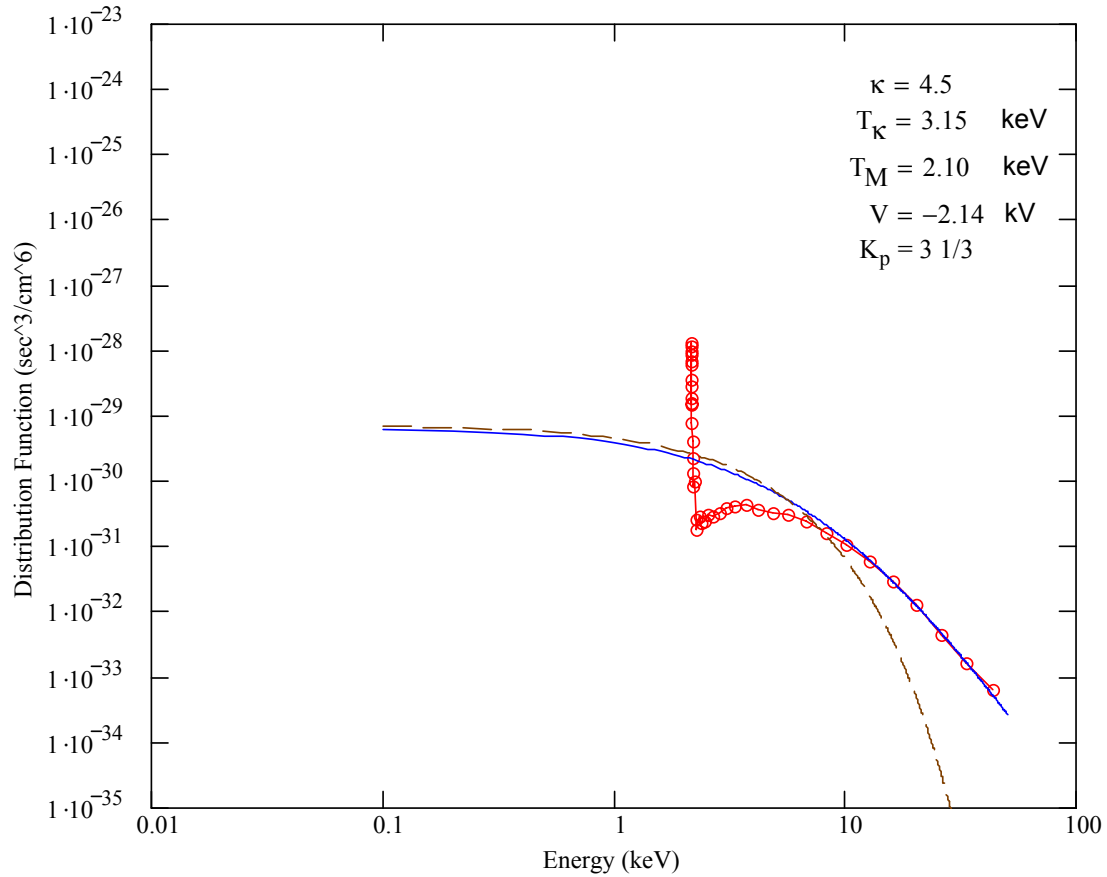

Figure 9   Electron Distribution Function vs. Electron Energies for LANL 1994-084 Data taken at 16.79 UT (23.69 LT) on 09 March 1999. Plotted are LANL data values (circles), kappa distribution (solid line), and Maxwellian Distribution (dash). (Data Courtesy of Michelle F. Thomsen, Los Alamos National Laboratory.)

IV. Analysis

This chapter presents an examination of an eclipse charging event which took place during one of the periods examined by Lai and Della-Rose (2001). This event was chosen since it is representative of significant charging that can occur during eclipse, and the pattern of charging is consistent with other charging events of this type in the data we examined. The data presented will provide a basis for evaluating the value of the kappa distribution, as compared to the Maxwellian distribution, as a predictor of the onset of significant spacecraft charging.

As noted in Section 3.3, in the interest of minimizing subjectivity, electron number densities were calculated for use in conjunction with visual fits. The number densities were calculated from Equations (33), (34), and (35). These number densities were used to help narrow down the best temperature fit corresponding to the chosen kappa value. The kappa value was selected based on its sufficiency for modeling the slope of the high-energy part of a given particle distribution.

4.1 Principal Features of Concern

As the electron energy distribution shifts to higher energies, the slope of the tail with energies $> 10\ keV$ decreases, indicating that smaller kappa values are associated with more high-energy electrons. These low kappa values are positively correlated to higher potentials, as expected. This follows since, for incident electrons in region III of the secondary emission curve, a large potential must develop before a balance between incoming and outgoing currents will be achieved, resulting in a steady-state potential. Conversely, large kappa values tend to signify lower distributions of high-energy electrons, resulting in lower spacecraft potentials. This is evident in Figures 8 and 9, and it is consistent with the explanation given by Hastings and Garrett (1996:70). These incident, high-energy electrons characterized by the tail continue to increase the spacecraft surface potential until a steady-state potential is reached.

In summary, if our kappa fit of the data produces relatively "small" kappa values (less than about 15.5), then we can conclude that the plasma exhibits a high-energy tail not captured by a Maxwellian distribution. Recall that as $\kappa \to \infty$, the kappa distribution function becomes Maxwellian. So for the purpose of this research, we consider that when $\kappa \geq 15.5$, the distribution is essentially a Maxwellian distribution.

4.2 Observations of Spacecraft Charging on 14 March 1999

In this section, we review a spacecraft charging event, reflected by LANL 1991-080, 1994-084, and 1997A data, which occurred on 14 March 1999. Each spacecraft measured significant ($> 1\ kV$) charging somewhere in the timeframe 16-24 UT. For reference, plots of spacecraft potential and temperature are displayed for each satellite. Each of these plots also highlights the period of eclipse, denoted by a black line at $-2\ kV$. In each case, the eclipse period is near midnight local time.

A typical eclipse charging scenario can be inferred from these graphs. Notice that the spacecraft potentials are low (~ 0) initially, then a sharp rise in temperature is apparent. This sharp temperature increase is accompanied by an obvious increase in spacecraft potential. From these figures, it is clear that the most significant charging occurred in or near eclipse. The 3-hourly K_p indices were 3, 3, and $3\frac{2}{3}$ at 18, 21 and 24 UT, respectively.

For reference, we note that the critical temperature for significant charging in a Maxwellian plasma is 1.34 keV when assuming non-activated CuBe as a material. Lai and Della-Rose determined that non-activated CuBe spacecraft material was suggested by the critical temperatures they observed from the LANL data they examined (2001:926). We must bear this in mind as we examine the charging on the satellites. Recall that significant charging does not take place every time spacecraft enter eclipse, but when it does, the spacecraft potentials occasionally reach levels that can cause damage to components.

4.2.1 Satellite 1991-080. Figure 10 is a graph of the potentials and electron temperatures for satellite 1991-080 during the timeframe 16-24 UT. This graph also highlights the dependence of potentials on temperature once the charging begins. Observe that the charging event commences around 21 UT and continues past local midnight (23.47 UT). This satellite continued to charge into the morning hours (UT and local time) of 15 March 1999. Finally, it is evident that the spacecraft potential reaches its maximum value during this charging event while the spacecraft is in eclipse.
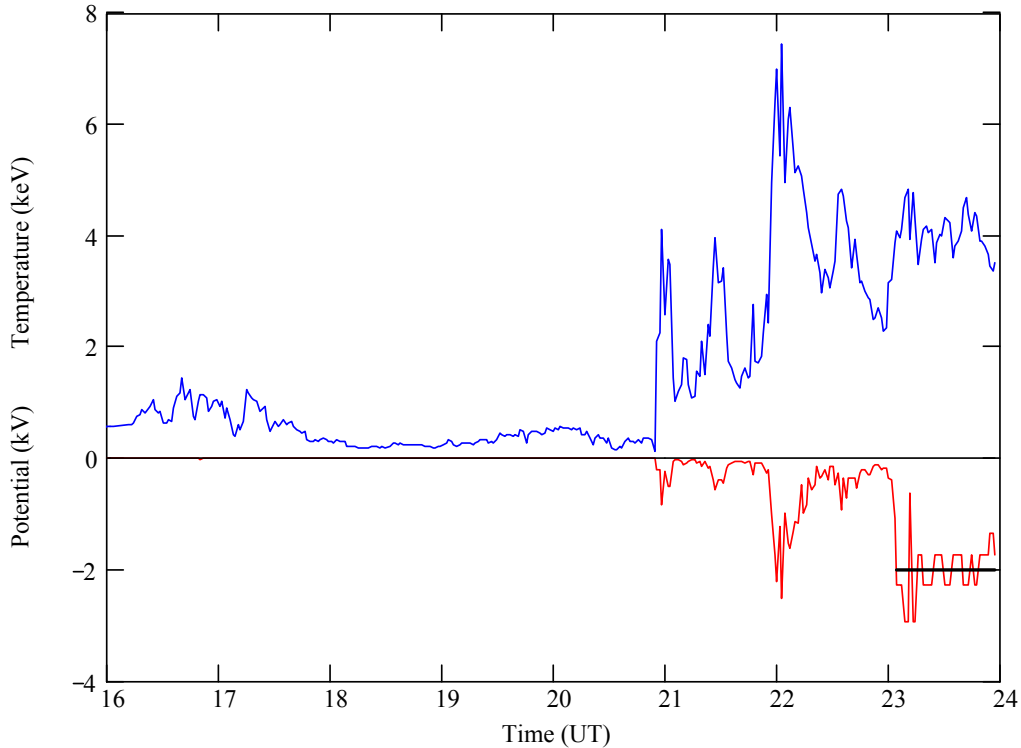
Figure 10   Spacecraft Potential and Electron Temperature Curves for LANL 1991-080 on 14 March 1999/16-24 UT. The black line at -2 kV potential shows the period of eclipse. (Data Courtesy of Michelle F. Thomsen, Los Alamos National Laboratory.)

Figures 11 and 12 show LANL 1991-080 data for 20.90 UT (21.42 LT), near the onset of the charging event, and about two hours before the satellite enters eclipse.

Figure 11   Electron Distribution Function vs. Electron Energy at 20.90 UT (21.42 LT) on 14 March 1999 from LANL 1991-080 Data. Displayed are the Data Derived (circles), the kappa (solid), and the Maxwellian (dash) Distribution Functions. (Data Courtesy of Michelle F. Thomsen, LANL.)

The fit in Figure 12 was obtained by increasing the Maxwellian temperature until a reasonable match with the distribution function for the key channels, with respect to charging, was achieved. Both large kappa ($\kappa = 15.5$) and Maxwellian distributions give good fits at energies below 10 keV. However, the spacecraft potential

is low, and the high-energy ($\geq 10 \ keV$) distribution function values are inconsequential with respect to charging. Therefore, as we might expect, a Maxwellian distribution does an adequate job in this case.

Figure 12   Electron Distribution Function vs. Electron Energy at 20.90 UT (21.42 LT) on 14 March 1999 from LANL 1991-080 Data. The Fit is with Respect to the Maxwellian Temperature. Displayed are the Data Derived (circles) and the Maxwellian (dash) Distribution Functions. (Data Courtesy of Michelle F. Thomsen, LANL.)

Figure 13, which shows data at 20.92 UT (21.45 LT), is the next measurement (about 72 seconds later). Note that the predicted Maxwellian critical temperature and the $\kappa = 10.5$ predicted critical temperature of 1.38 keV are both exceeded by

the fitted kappa temperature. This is consistent with the theory that significant charging can occur above the critical temperature. One key feature of this graph is that the kappa fit is noticeably better than the Maxwellian fit in the high-energy part of the distribution, even if the Maxwellian temperature is increased. This graph, and those with potentials larger than about 20 eV that follow, are solid examples of the energy shift described in Section 3.3. The correlation between this energy shift, qV, and the associated spacecraft potential, V, stands out in each case.
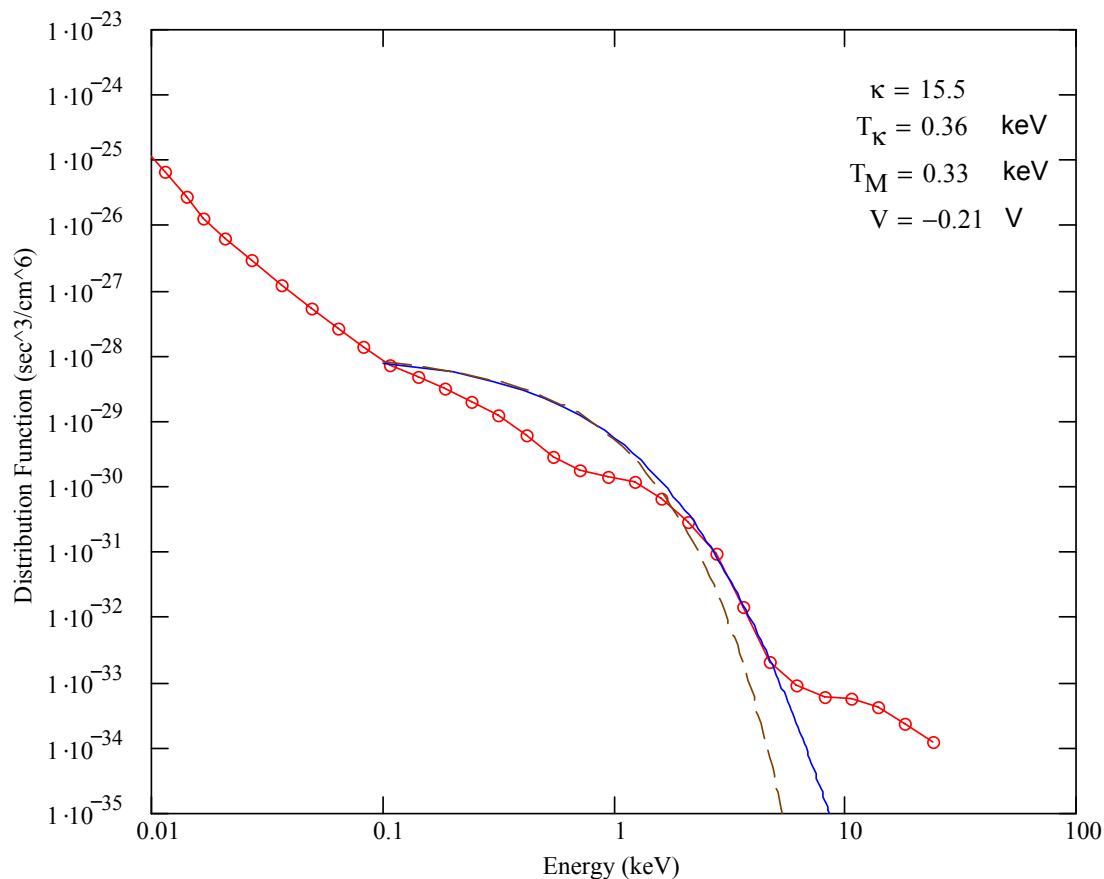

Figure 13   Electron Distribution Function vs. Electron Energy at 20.92 UT (21.45 LT) on 14 March 1999 from LANL 1991-080 Data. Displayed are the Data Derived (circles), the kappa (solid), and the Maxwellian (dash) Distribution Functions. (Data Courtesy of Michelle F. Thomsen, Los Alamos National Laboratory.)

Figure 14, valid at 22.90 UT (23.45 UT), is a snapshot just before the spacecraft enters eclipse. Here, the potential is low, and the kappa value remains high (nearly Maxwellian). Using $\kappa = 15.5$, the kappa current balance equation returns a critical temperature of 1.36 keV – well above that estimated from the Figure 11 kappa fit. On the other hand, it is well below that from the kappa fit in Figure 14, just before the spacecraft charges to a relative (negative) potential of 1 kV. Recall that 1 kV is the criteria we identified earlier to denote the lower limit of significant charging.
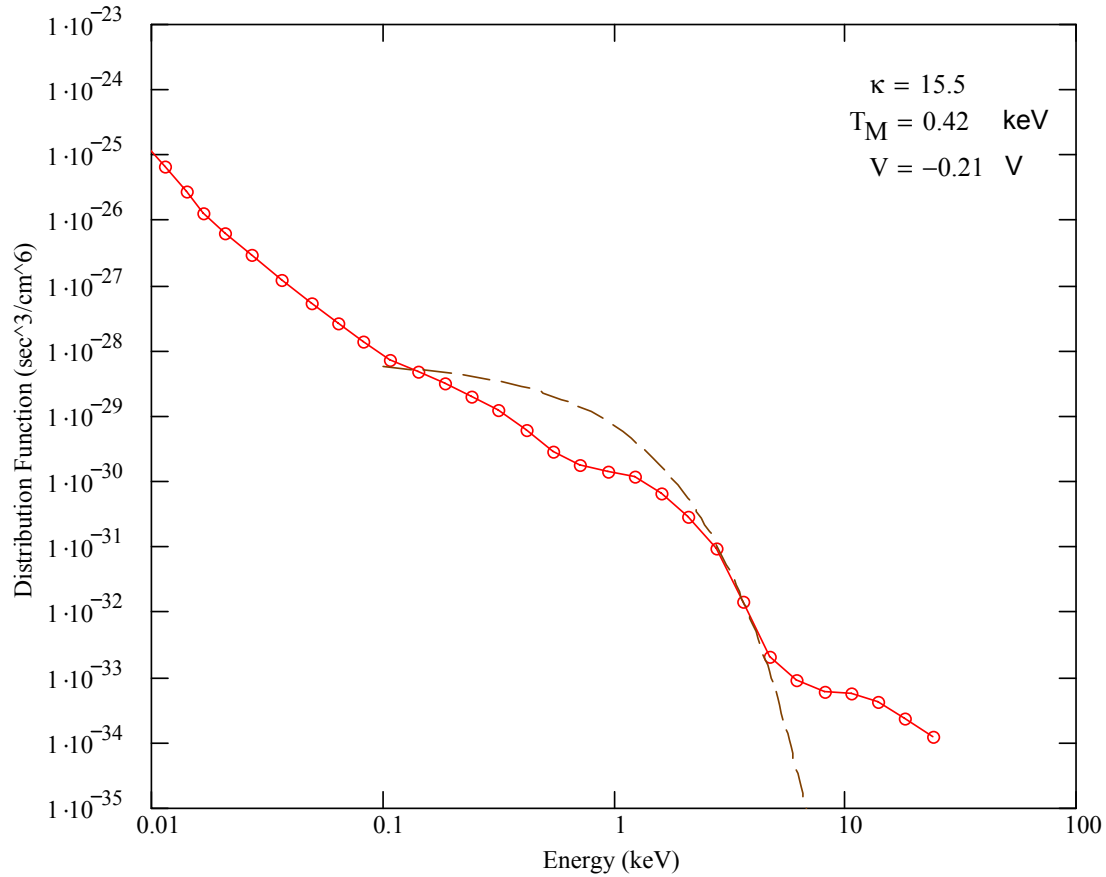

Figure 14   Electron Distribution Function vs. Electron Energy at 22.90 UT (23.43 LT) on 14 March 1999 from LANL 1991-080 Data. Displayed are the Data Derived (circles), the kappa (solid), and the Maxwellian (dash) Distribution Functions. (Data Courtesy of Michelle F. Thomsen, Los Alamos National Laboratory.)

46

Figures 15 and 16 are plots of the distribution functions at 23.07 UT (23.60 LT), shortly after the spacecraft moved into eclipse. These figures provide solid examples of how the high-energy portion of the distribution increases, and the spacecraft potential is high as well. The unexpected aspect of this data plot is that, as shown in Figure 16, the Maxwellian actually gives a slightly better fit at the high-energy tail.
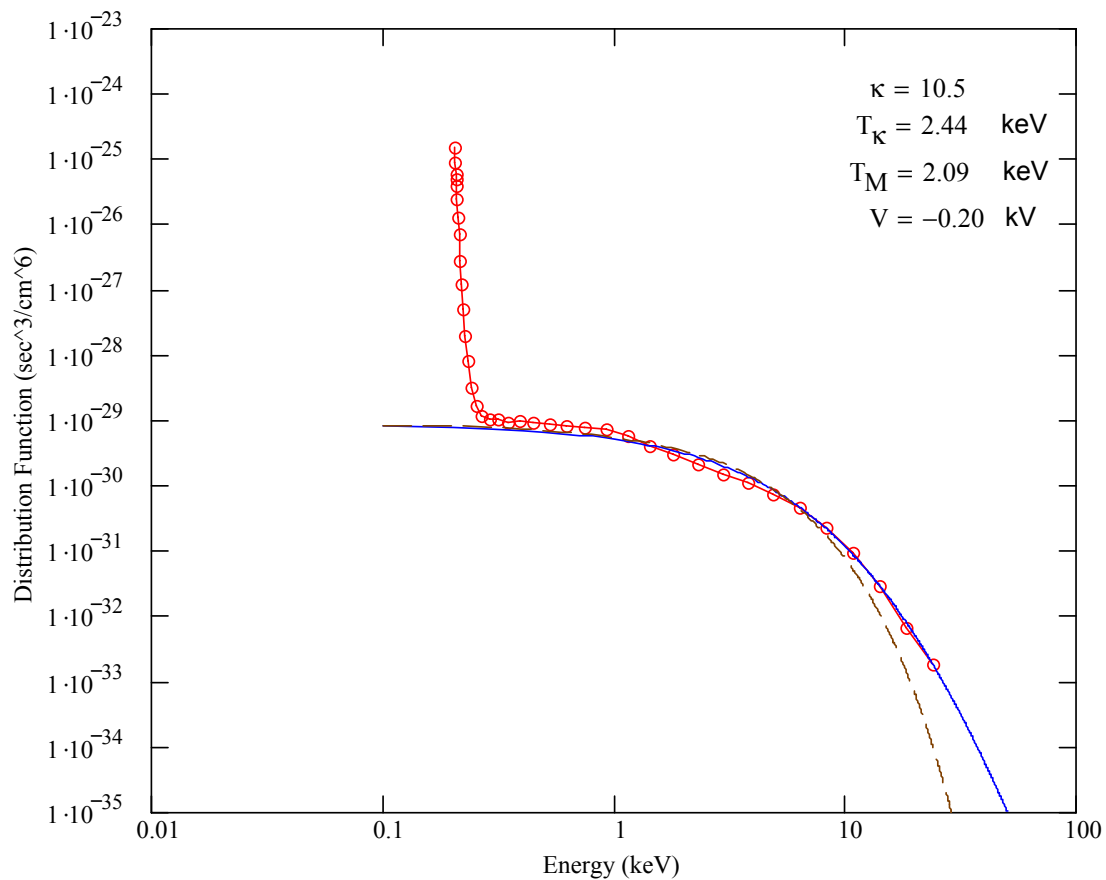

Figure 15   Electron Distribution Function vs. Energy at 23.07 UT (23.60 LT) on 14 March 1999 from LANL 1991-080 Data. Displayed are the Data Derived (circles), the kappa (solid), and the Maxwellian (dash) Distribution Functions. (Data Courtesy of Michelle F. Thomsen, Los Alamos National Laboratory.)

κ = 15.5
T_M = 3.25 keV
V = −2.26 kV

Figure 16   Electron Distribution Function vs. Energy at 23.07 UT (23.60 LT) on
14 March 1999 from LANL 1991-080 Data Showing that the Maxwellian
Distribution (unexpectedly, in this case) Fits the High Energy Part of
the Distribution Better than the kappa Distribution Does. Displayed
are the Data Derived (circles) and the Maxwellian (dash) Distribution
Functions. (Data Courtesy of Michelle F. Thomsen, Los Alamos Na-
tional Laboratory.)

4.2.2   Satellite 1994-084.   Figure 17 is a graph of the spacecraft potentials
and temperatures for satellite 1994-084, valid 16-24 UT. Local midnight for this data
set occurred at 17.10 UT. We can clearly see the surge in potential accompanying
the jump in electron temperature. Consistent with observations for 1991-080, the

48

peak potential for 1994-084 was reached shortly after the spacecraft entered eclipse. In contrast to the situation with 1991-080 (ref. Figure 10), where the charging event began a few hours before the spacecraft was in eclipse, the charging for 1994-084 initiated only about an hour before eclipse, at about 16.15 UT (23.05 LT). In this instance, the charging regime continued for several hours after eclipse. The reasons for this difference in course of events were not addressed during this research.
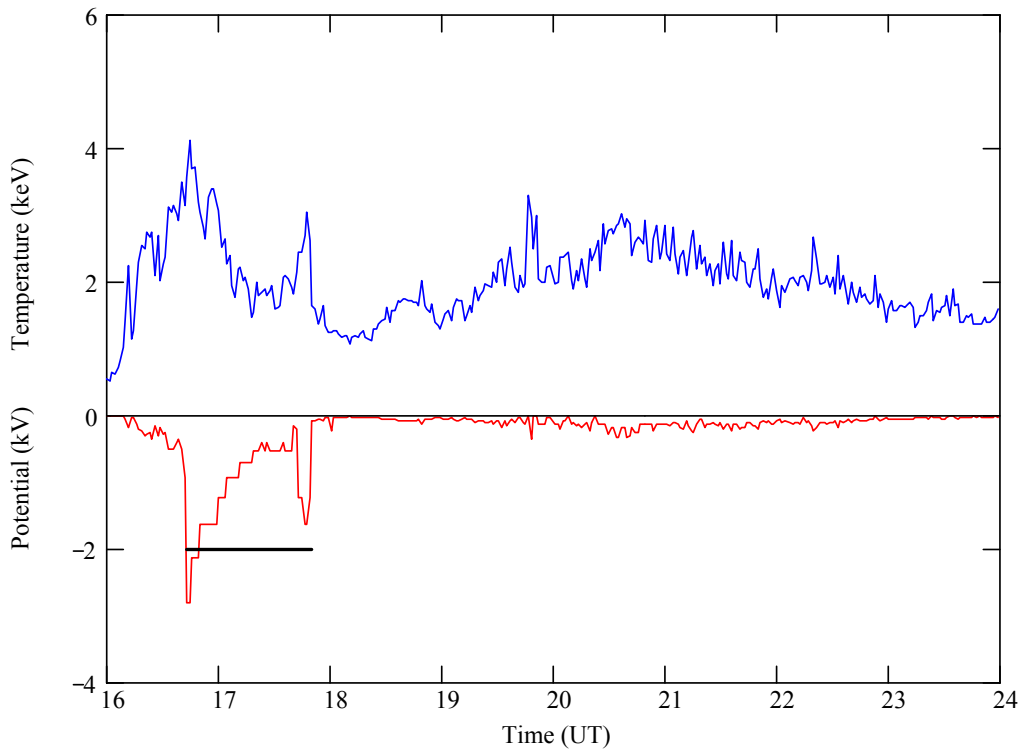
Figure 17   Spacecraft Potential and Electron Temperature Curves for LANL 1994-084 on 14 March 1999/16-24 UT. The black line at -2 kV potential shows the period of eclipse. (Data Courtesy of Michelle F. Thomsen, Los Alamos National Laboratory.)

Figures 18 and 19 show LANL 1994-084 data at 16.02 UT (22.92 LT), before eclipse begins and near the onset of the charging event. Using the same fitting procedures as in Figures 11 and 12, both the kappa and the Maxwellian distributions

49

give good fits at energies below 10 keV, but the kappa fit in Figure 18 is clearly superior overall in this case. This result contrasts with that for the first data plots of satellite 1991-080.
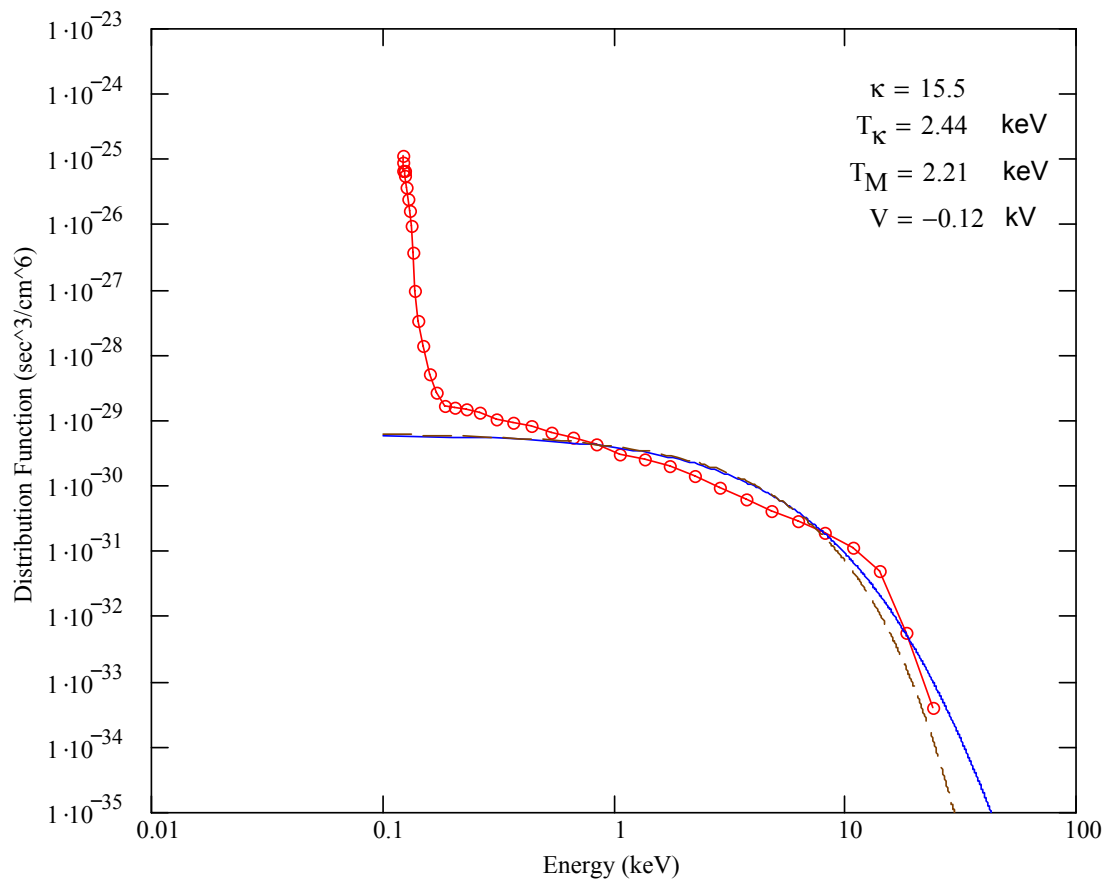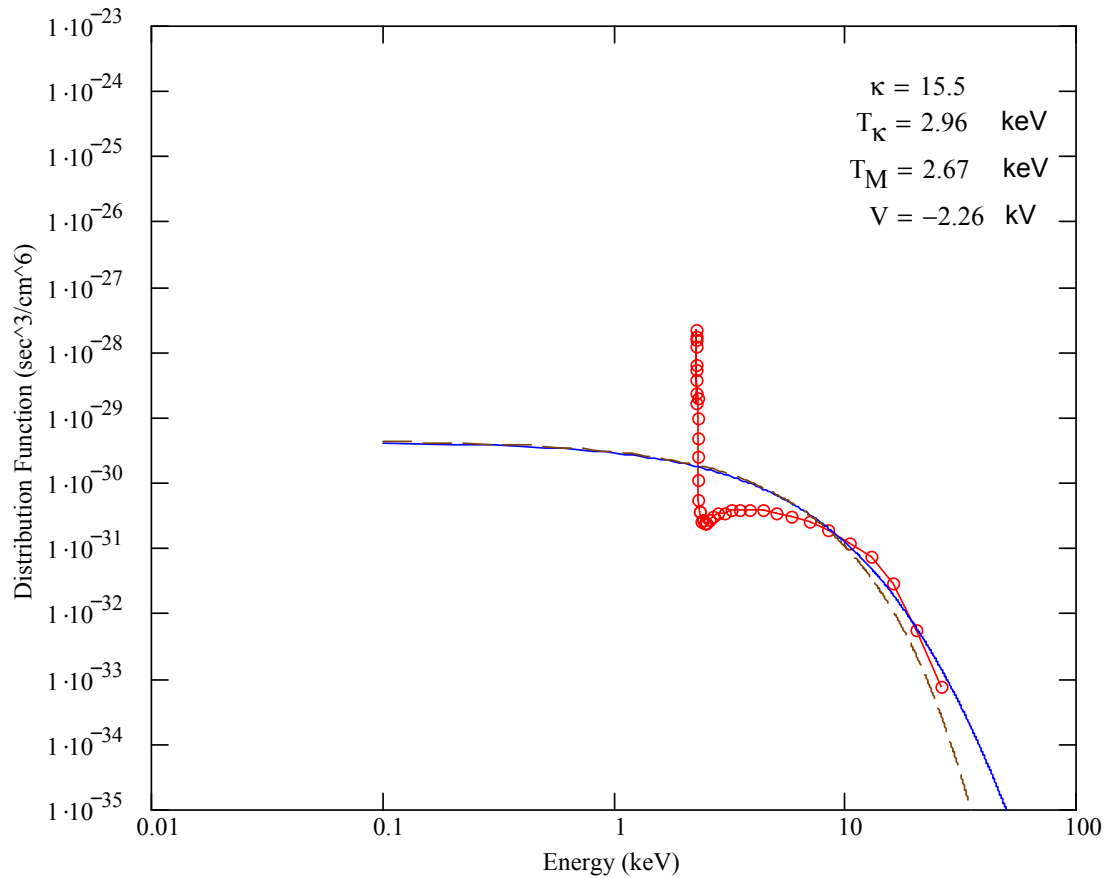

Figure 18   Electron Distribution Function vs. Energy at 16.02 UT (22.92 LT) on 14 March 1999 from LANL Satellite 1994-084 Data. Displayed are the Data Derived (circles), the kappa (solid), and the Maxwellian (dash) Distribution Functions. (Data Courtesy of Michelle F. Thomsen, Los Alamos National Laboratory.)
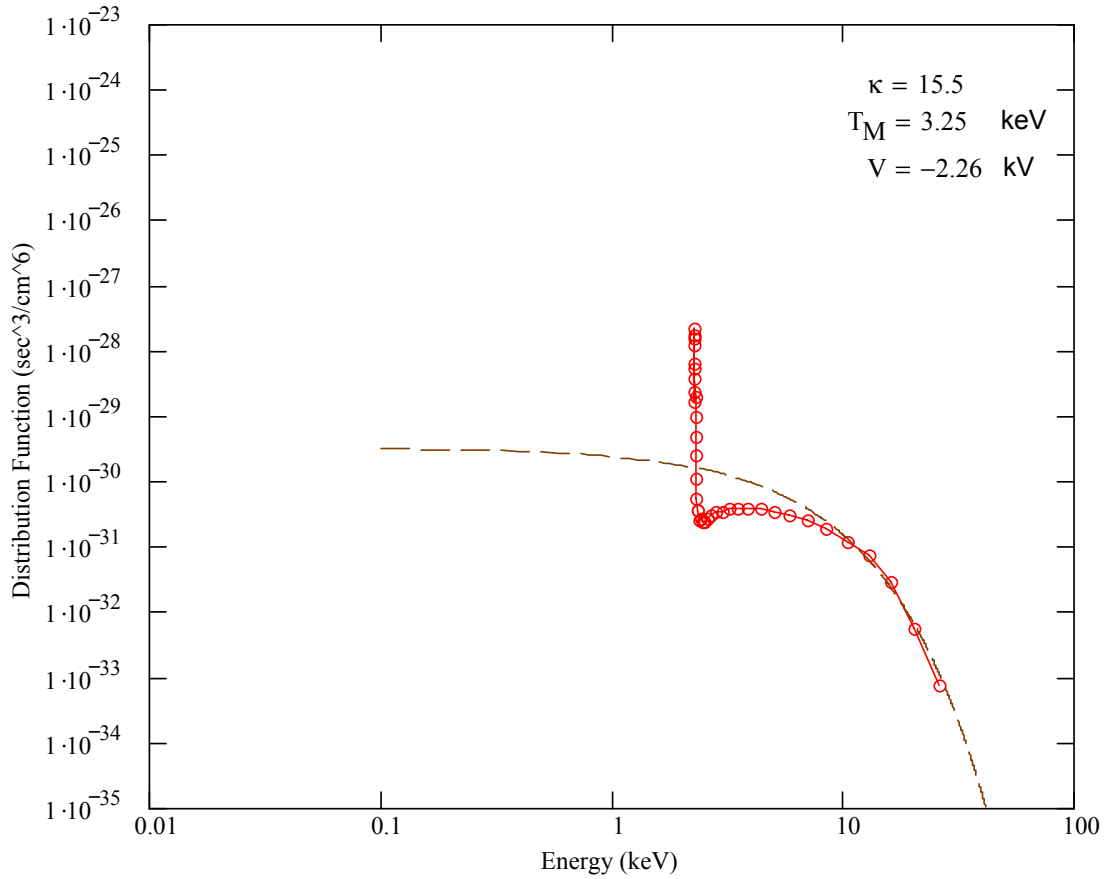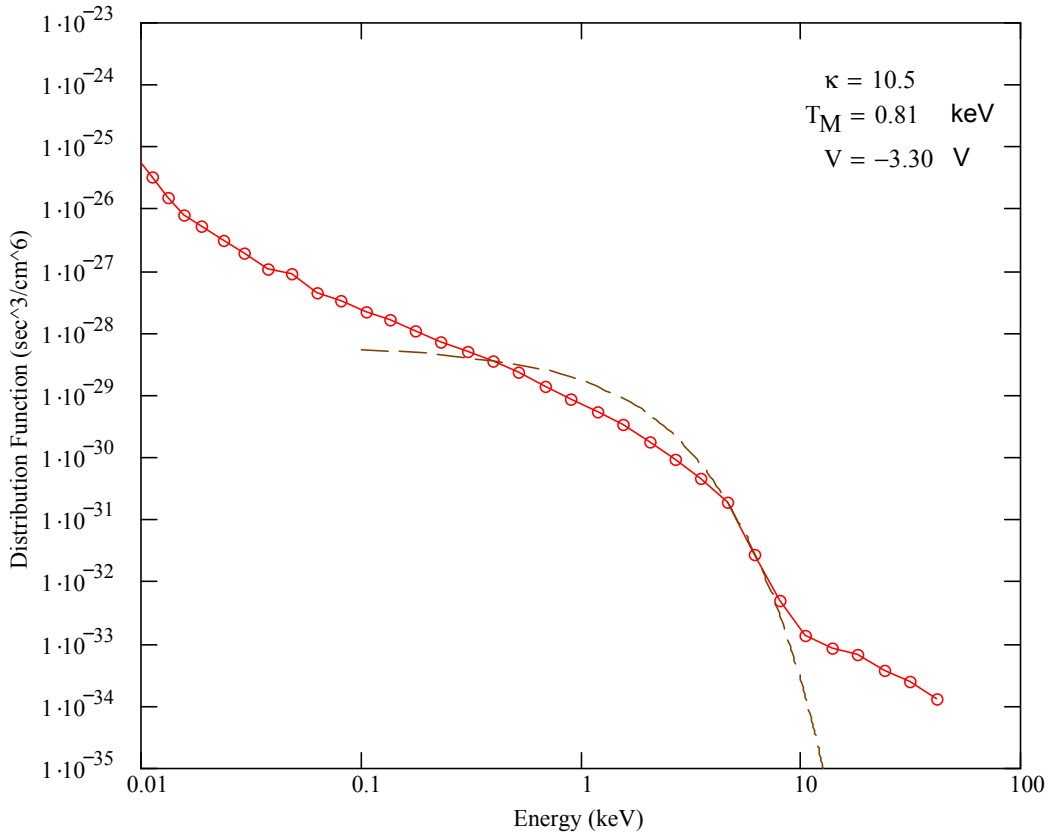
Figure 19   Electron Distribution Function vs. Energy at 16.02 UT (22.92 LT) on 14 March 1999 from LANL 1994-084 Data. The Fit is with Respect to the Maxwellian Temperature. Displayed are the Data Derived (circles) and the Maxwellian (dash) Distribution Functions. (Data Courtesy of Michelle F. Thomsen, Los Alamos National Laboratory.)

Figure 20, valid at 16.16 UT (23.06 LT), about 9 minutes later, shows a potential of -59 V. Observe that, like Figure 13, it shows that the critical temperatures predicted by the kappa and Maxwellian current balance equations have been exceeded by the temperature derived from the fitting procedure. Again, this is consistent with the charging theory. The kappa current balance equation forecasts a critical temperature of $T_\kappa = 1.40$ keV for $\kappa = 7.5$.

A notable feature of the next three data plots, including Figure 20, is that the kappa distribution clearly does a superior job of representing the measured distribution functions. Notice how the slope of the high-energy data is picked up by the kappa distribution in all cases. Moreover, as the potential increases, the slope decreases, and the kappa values follow suit. Even the low voltage case was better depicted by the kappa curves than by the Maxwellian. This fact sets these measurements apart from those on the other two spacecraft.

Figure 20   Electron Distribution Function vs. Electron Energy at 16.16 UT (23.06 LT) on 14 March 1999 from LANL 1994-084 Data. Displayed are the Data Derived (circles), the kappa (solid), and the Maxwellian (dash) Distribution Functions. (Data Courtesy of Michelle F. Thomsen, Los Alamos National Laboratory.)

Figure 21 is a snapshot, at 16.62 UT (23.52 LT), just before the spacecraft enters eclipse and reaches a peak potential. Observe that the kappa value has dropped down to 5.5, corresponding to the considerable increase (by an order of magnitude) of the high-energy end of the distribution function.
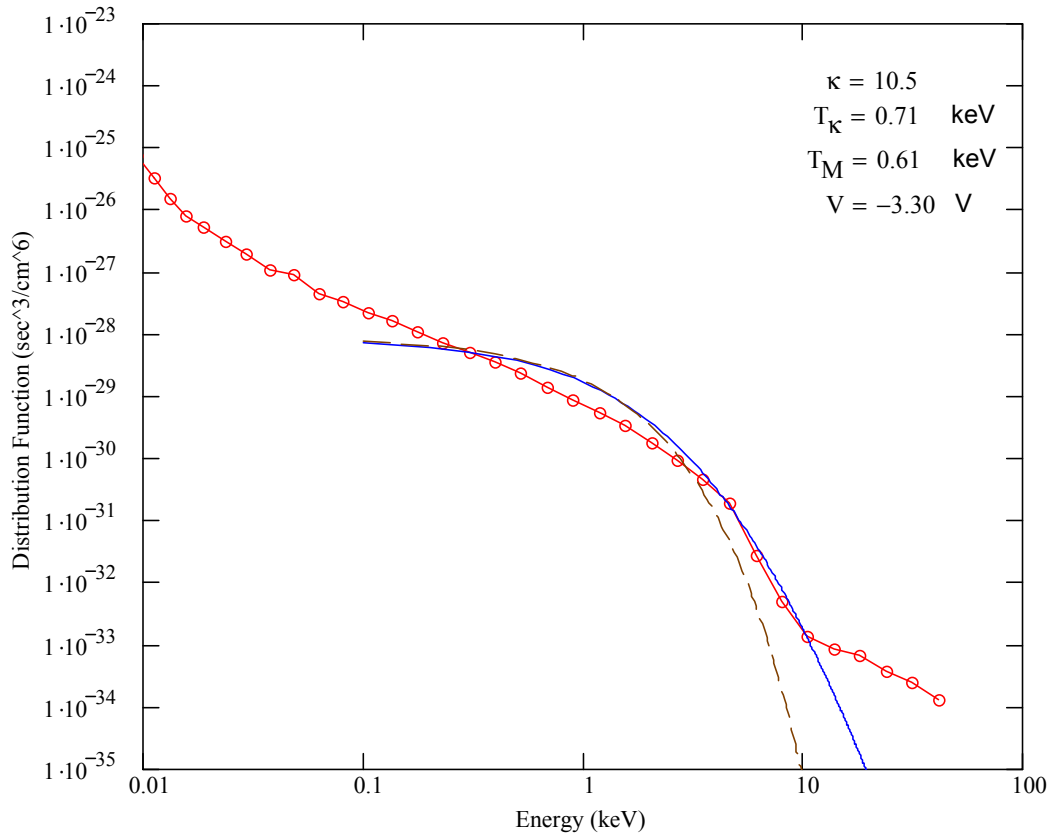

Figure 21   Electron Distribution Function vs. Electron Energy at 16.62 UT (23.52 LT) on 14 March 1999 from LANL 1994-084 Data. Displayed are the Data Derived (circles), the kappa (solid), and the Maxwellian (dash) Distribution Functions. (Data Courtesy of Michelle F. Thomsen, Los Alamos National Laboratory.)

Figure 22 is a plot of the distribution functions at 16.71 UT (23.61 LT). This is the first reading taken during the time the satellite is in eclipse. Using $\kappa = 4.5$, the kappa current balance equation returns a critical temperature of 1.46 keV. This is

far below the corresponding temperatures that make the curves fit well for Figures 21 and 22. This contrasts with using $\kappa = 10.5$ in Figure 18, which returns a critical temperature of 1.38 keV – well above that which produced a good fit at that time.

Figure 22 Electron Distribution Function vs. Energy at 16.71 UT (23.61 LT) on 14 March 1999 from LANL 1994-084 Data. Displayed are the Data Derived (circles), the kappa (solid), and the Maxwellian (dash) Distribution Functions. (Data Courtesy of Michelle F. Thomsen, Los Alamos National Laboratory.)

4.2.3 Satellite 1997A. Finally, we examine LANL 1997A data. One clear difference between this and the other spacecraft is that 1997A underwent significant charging in the middle of the period 16-24 UT. Notice that charging began almost three hours before the satellite migrated into eclipse, and the event continued for

several hours afterward. This pattern is consistent with the scenario observed for satellite 1991-080. Also, similar to 1991-080, the satellite was at significant potentials for a large part of the time it was in eclipse.
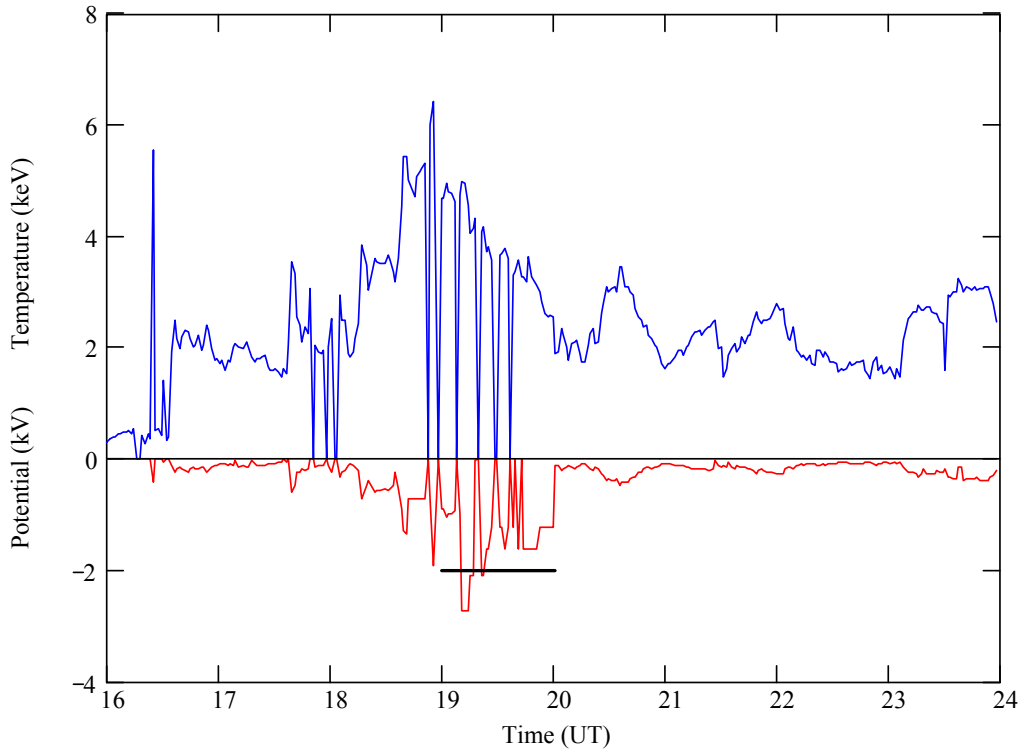
Figure 23   Spacecraft Potential and Electron Temperature Curves for LANL 1997A on 14 March 1999/16-24 UT. The black line at $-2\ kV$ potential shows the period of eclipse. (Data Courtesy of Michelle F. Thomsen, Los Alamos National Laboratory.)

Figures 24 and 25 depict the situation at 16.38 UT (21.05 LT), shortly after the onset of charging and almost three hours before eclipse. Here, the fitting technique is the same as for Figures 11 and 12. The kappa fit is only marginally better than the Maxwellian in this case, especially considering that only a small number of data points (energy channels) provide a good visual fit. But neither the kappa critical temperature of $T_\kappa = 1.43\ keV$ nor the Maxwellian critical temperature of $T_M = 1.34$

keV is reached in these fits. There is no major difference among the patterns in these two plots and those from the other spacecraft where low potentials near the beginning of the charging regimes are present.
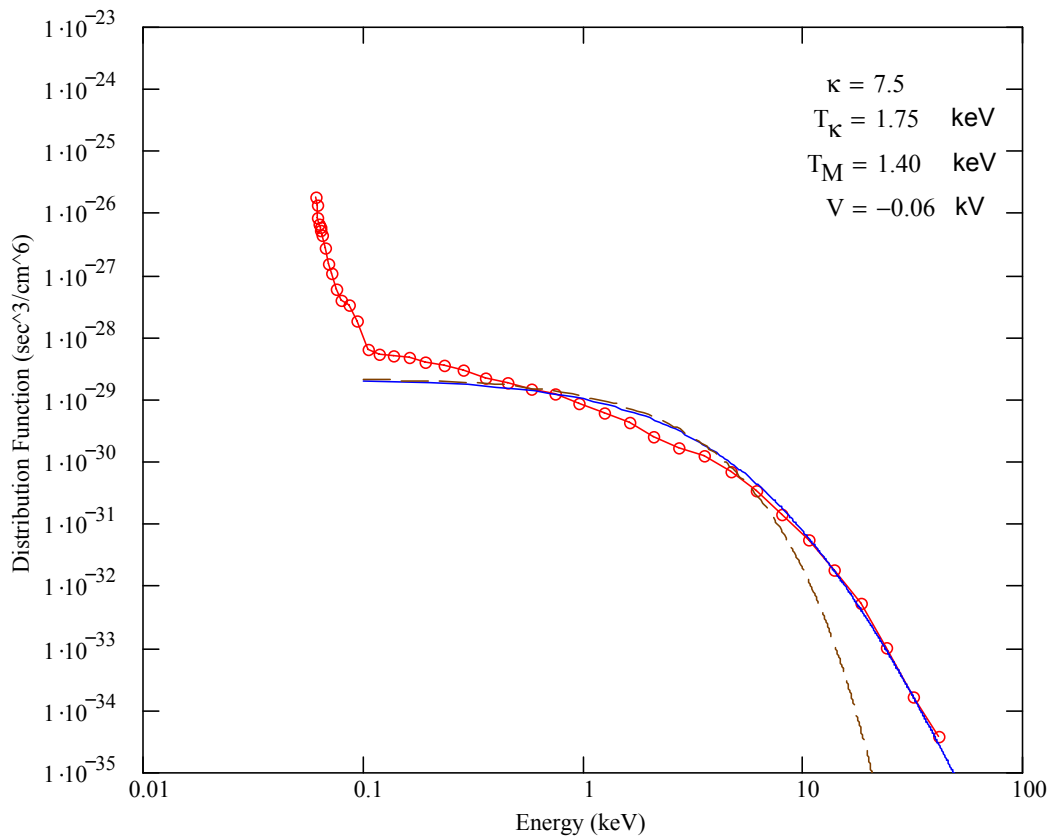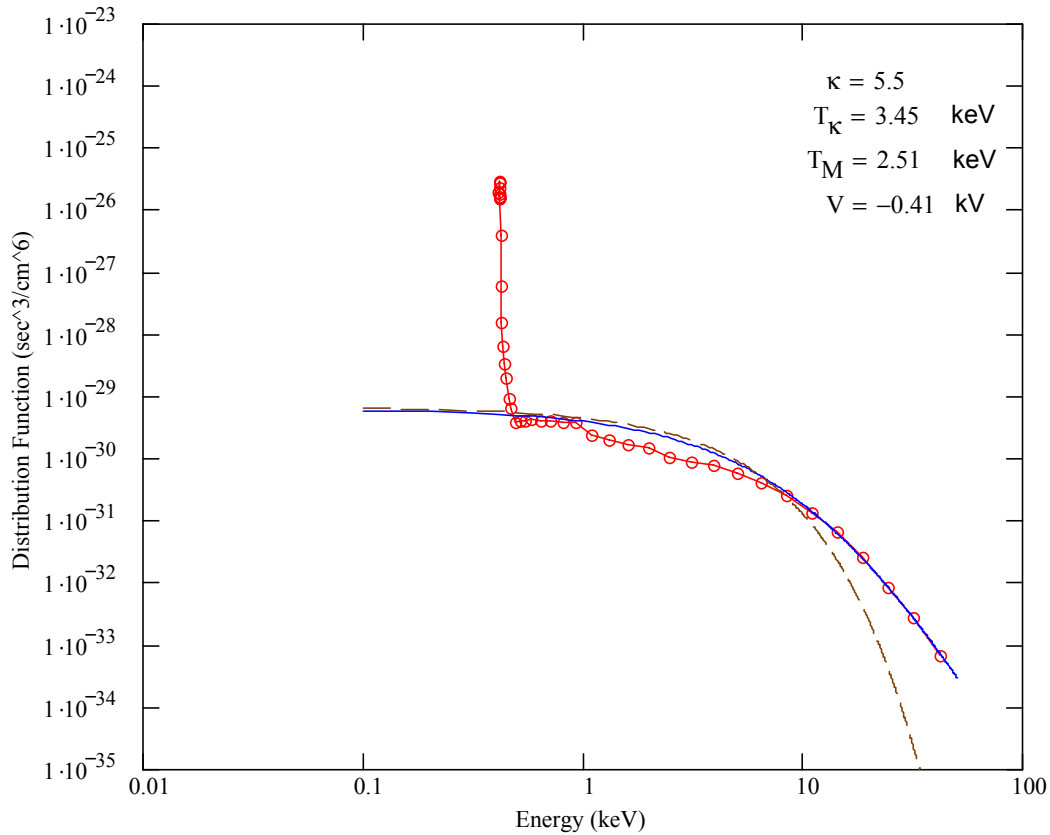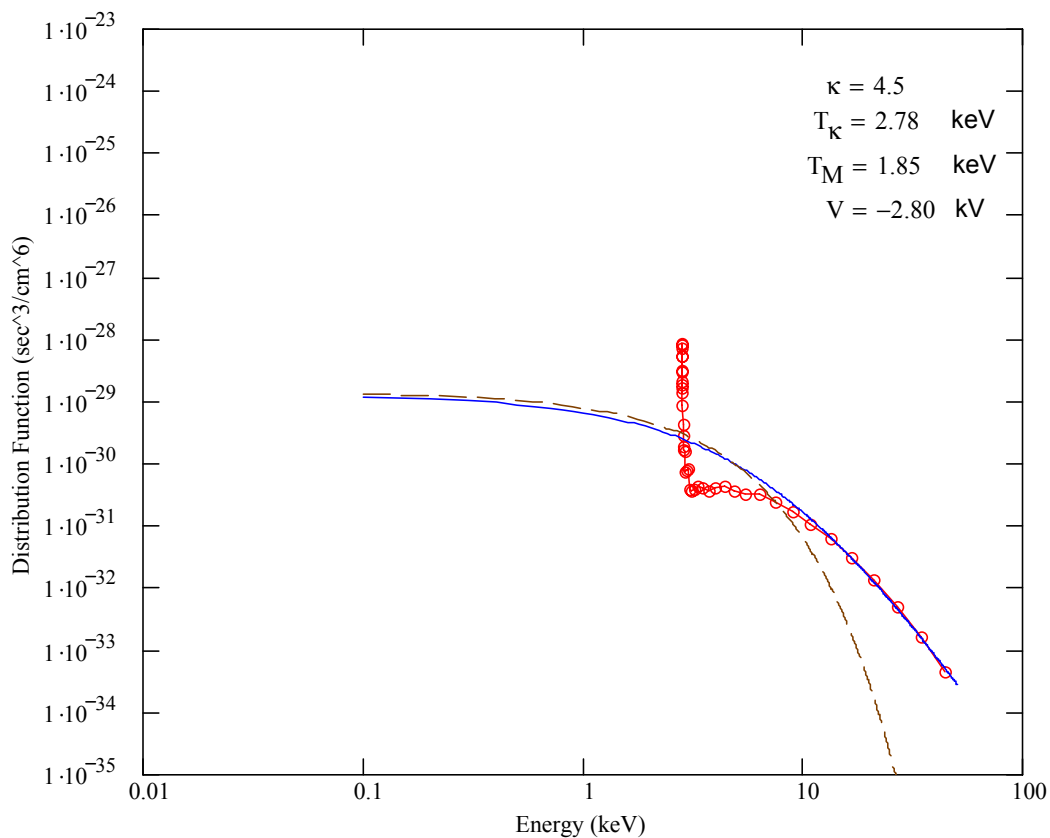

Figure 24   Electron Distribution Function vs. Energy at 16.38 UT (21.05 LT) on 14 March 1999 from LANL 1997A Data. Displayed are the Data Derived (circles), the kappa (solid), and the Maxwellian (dash) Distribution Functions. (Data Courtesy of Michelle F. Thomsen, Los Alamos National Laboratory.)
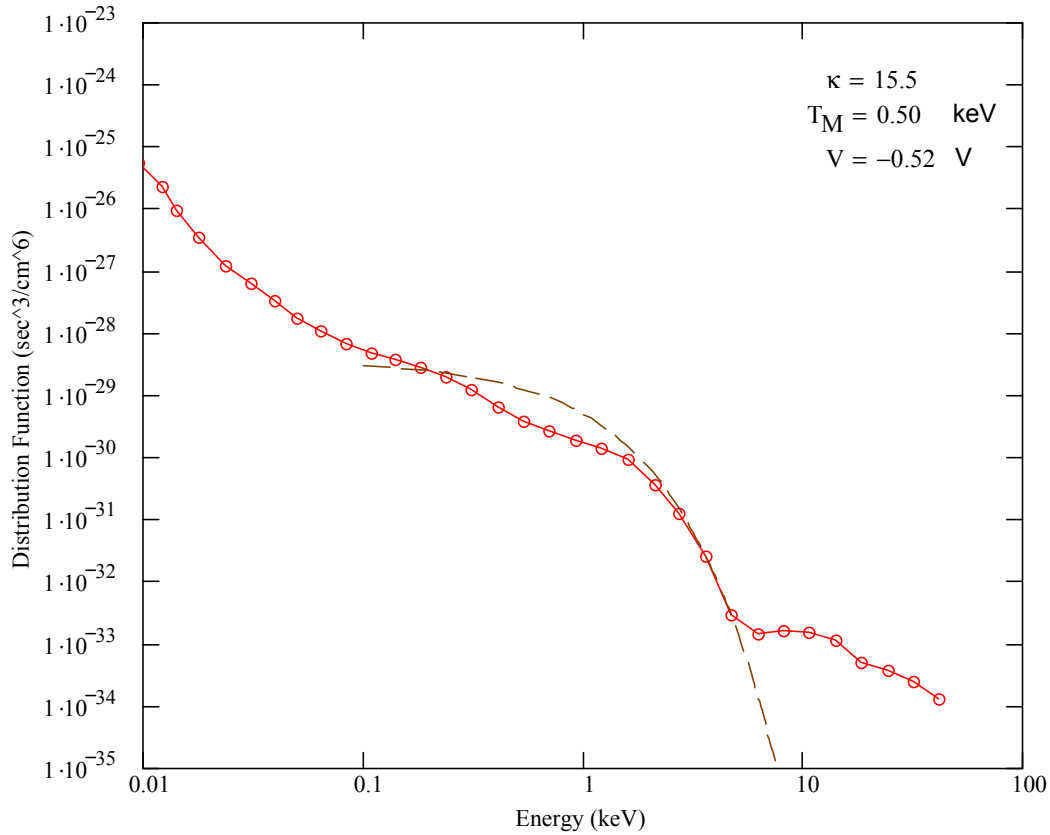
Figure 25   Electron Distribution Function vs. Energy at 16.38 UT (21.05 LT) on 14 March 1999 from LANL 1997A Data. The Fit is with Respect to the Maxwellian Temperature. Displayed are the Data Derived (circles) and the Maxwellian (dash) Distribution Functions. (Data Courtesy of Michelle F. Thomsen, Los Alamos National Laboratory.)

The distribution in Figures 26 and 27, valid at 16.50 UT (21.17 LT), requires a large kappa value to obtain a good fit. Notice that the Maxwellian temperature is very close to the kappa temperature, and the Maxwellian curve already shows promise for a good fit. This result is in spite of the fact that the potential is already at -45 V. It is worthwhile to point out that the predicted kappa temperature is $T_\kappa = 1.365$ keV at $\kappa = 15.5$. So even at this charging level, the critical temperature is not met or exceeded.

Figure 26   Electron Distribution Function vs. Electron Energy at 16.50 UT (21.17
            LT) on 14 March 1999 from LANL 1997A Data. Displayed are the
            Data Derived (circles), the kappa (solid), and the Maxwellian (dash)
            Distribution Functions. (Data Courtesy of Michelle F. Thomsen, Los
            Alamos National Laboratory.)

However, the Maxwellian temperature that best fits the data (as shown in Figure 27) does exceed the Maxwellian critical temperature, even though this charging situation occurs in sunlight. This is consistent with our theory. We can increase kappa to a higher value, $\kappa = 25.5$, say, and obtain a fair fit at best with the critical temperature, $T_\kappa = 1.355\ keV$ being exceeded by a kappa fit temperature of $T_\kappa = 1.44$ keV. Overall, we can surmise that the Maxwellian is a better predictor of the critical temperature when compared to the kappa distribution for this example.
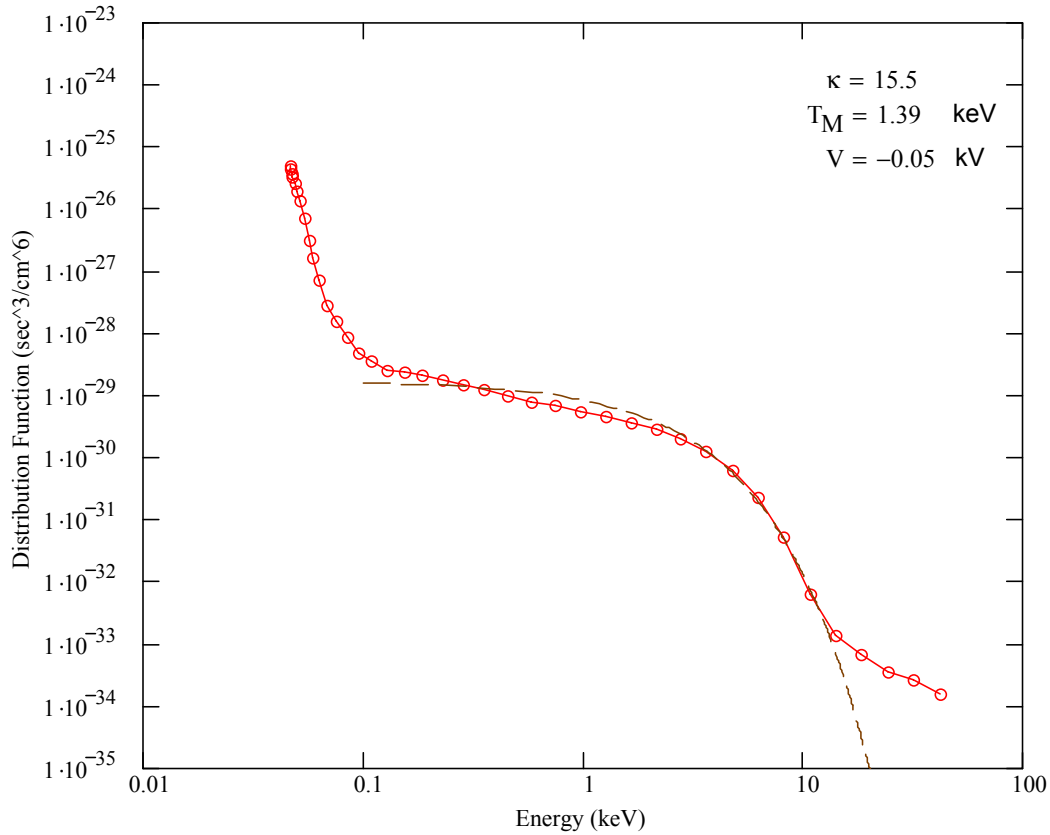
Figure 27   Electron Distribution Function vs. Electron Energy at 16.50 UT (21.17
            LT) on 14 March 1999 from LANL 1997A Data. The Fit is with Respect
            to the Maxwellian Temperature, and the Potential is -45 V. Displayed
            are the Data Derived (circles) and the Maxwellian (dash) Distribution
            Functions. (Data Courtesy of Michelle F. Thomsen, Los Alamos Na-
            tional Laboratory.)

Figure 28 shows the distribution functions at 16.98 UT (21.65 LT). At this
point, the potential has doubled as compared to the potential measured about 30
minutes before. This data plot exhibits a good kappa fit, and the critical tempera-
ture determined by the kappa value from the fit is well above the predicted critical
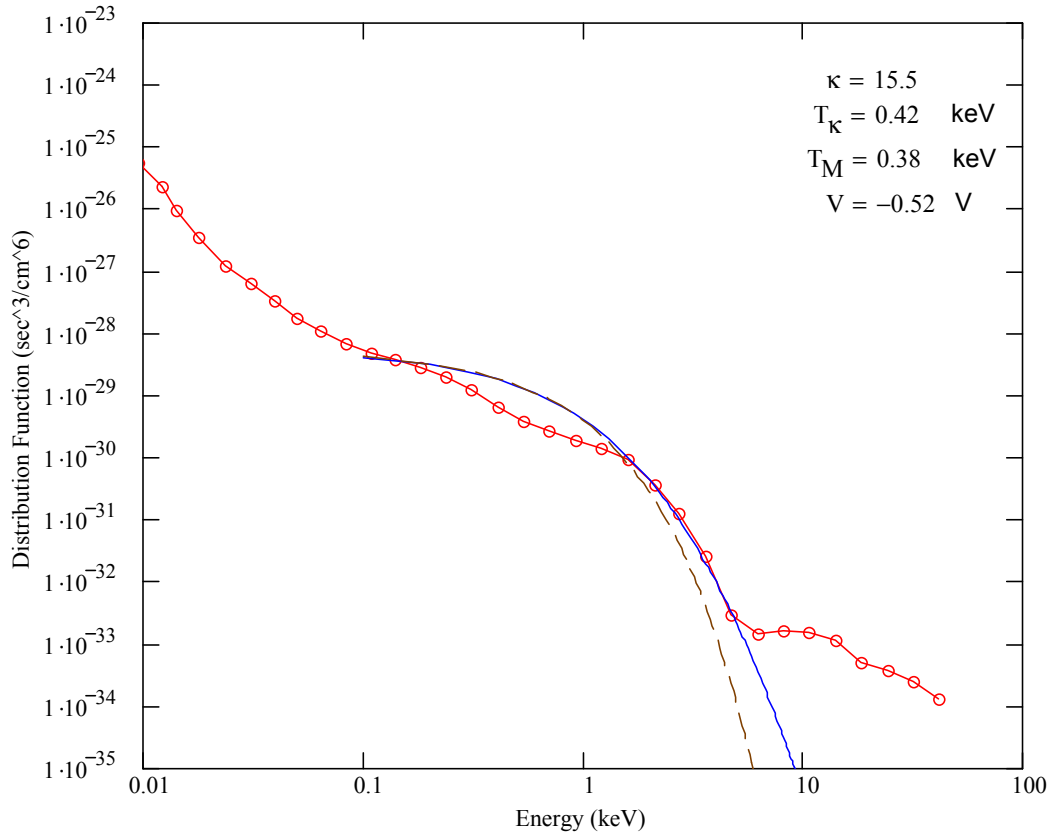temperature of 1.52 keV.

Figure 28   Electron Distribution Function vs. Electron Energy at 16.98 UT (21.65 LT) on 14 March 1999 from LANL 1997A Data. Displayed are the Data Derived (circles), the kappa (solid), and the Maxwellian (dash) Distribution Functions. (Data Courtesy of Michelle F. Thomsen, Los Alamos National Laboratory.)

Finally, Figure 29 shows the situation at 19.18 UT (23.84 LT), when the spacecraft is in eclipse. The peak potential for the day, $-2729\ V$, was reached at this time. As with satellite 1991-080, we see that this high potential requires a large kappa value to obtain a reasonable fit, and this part of the curve is better represented by a Maxwellian distribution at the high-energy end.
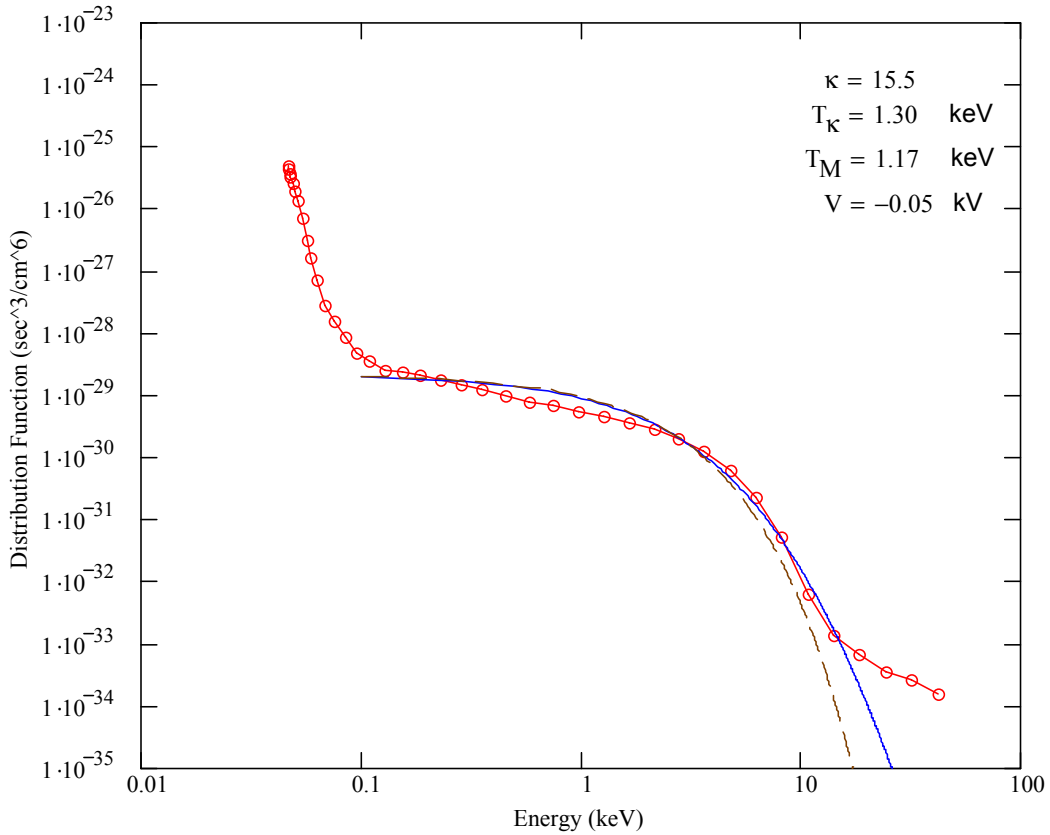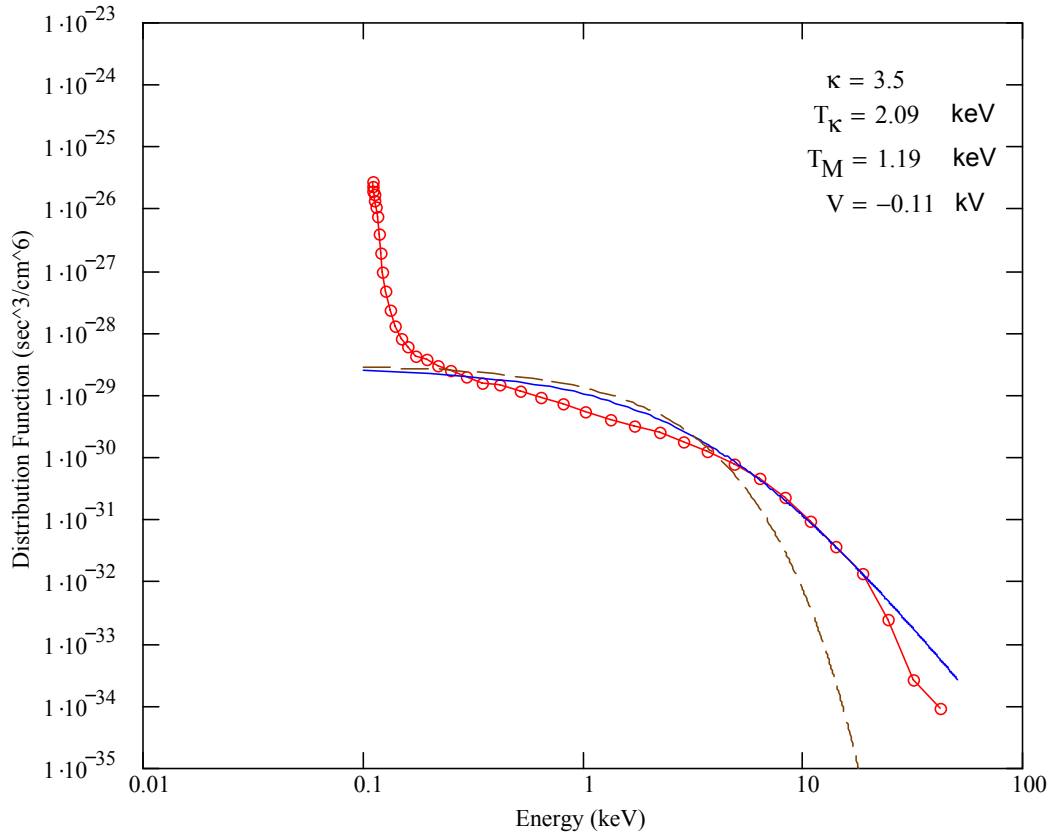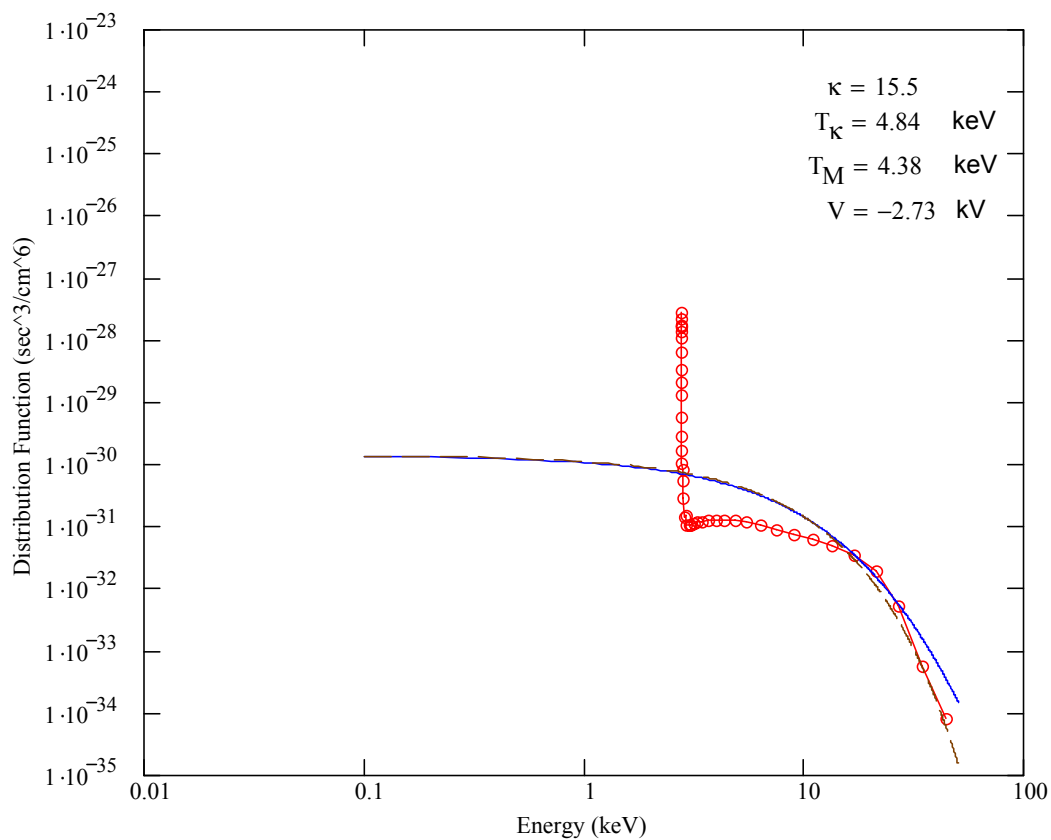
Figure 29   Electron Distribution Function vs. Energy at 19.18 UT (23.84 LT) on 14 March 1999 from LANL 1997A Data. Displayed are the Data Derived (circles), the kappa (solid), and the Maxwellian (dash) Distribution Functions. (Data Courtesy of Michelle F. Thomsen, Los Alamos National Laboratory.)

V. Results and Recommendations

5.1 Summary of Results

At charging onset in sunlight, there appears to be no non-Maxwellian, high-energy ($> 10 \ keV$) tail in most of the data we examined. The distributions where charging in sunlight occurred were nearly, if not distinctly, Maxwellian in shape. So application of the kappa distribution does not seem to contribute substantially in such cases. Additionally, the existence of such low-level charging cases does not seem to depend on the critical temperature charging predictions of Equation (6), which model only incoming, backscattered, and secondary electrons. Perhaps this is due to the fact that photoelectrons still dominate at this point. Recall that photoelectron flux was not incorporated into the current balance equation. However, by the time the spacecraft charges to more than about $-50 \ V$, the critical temperature criteria are exceeded for both the kappa and the Maxwellian data fits. This is true even for values of kappa less than 15.5, which is the threshold we used to delineate between non-Maxwellian and Maxwellian distributions.

None of the charging cases examined contradicted critical temperature theory – i.e., the existence of a critical temperature for significant ($> 1 \ kV$) charging was verified. When significant charging was observed, the kappa and the Maxwellian critical temperature predictions, based on the solutions of the respective current balance equations, were realized. So the critical temperature theory proved successful in this research.

In most cases studied, very low-level ($< 50 \ V$) charging can occur independent of critical temperature predictions. But such cases can occur in sunlight, where Equation (6) is not strictly valid. However, the current balance equation appeared to be applicable when potentials greater than $50 \ V$ were observed, even in sunlight. This held true for both the kappa and the Maxwellian forms of the equation.

Contrary to expectations, this research found no concrete benefit of using the kappa distribution over the Maxwellian in low-level charging cases. Many of the charging events commence under ambient plasma conditions that are modeled equally well by both the Maxwellian and the kappa distributions. This was especially apparent in the LANL 1991-080 and 1997A data. The 1994-084 data seemed to be an exception, but the reasons for this difference were not investigated in this research.

Some of the LANL distributions that corresponded to kilovolt charging were fit equally well by the Maxwellian distribution when compared to the kappa distribution (see, for example, Figures 15 and 16). This result seems unphysical since the ambient plasma is expected to be non-Maxwellian during large charging events. It may be due to the fact that a single distribution function is inadequate to model the space environment in such cases.

On the other hand, since the kappa distribution fits well with electron energies above 10 keV, it may be better than the Maxwellian distribution at determining the peak potentials that could be obtained. It has been noted that the linear dependence of potential on temperature is only approximate (Lai and Della-Rose, 2001:927). At higher potentials, the Maxwellian fails to determine the spacecraft charge, so the kappa may offer promise in this regard.

5.2   Recommendations

Based on the success of the critical temperature predictions, the Air Force Weather Agency (AFWA) should begin using these predictions for identifying GEO charging events. At this juncture, the Maxwellian current balance equation appears to be as successful as the kappa equation at predicting critical temperatures. Since it is also computationally simpler than the kappa equation, it should be the equation of choice until (if) a better tool comes along.

Determination of critical temperatures may require additional processing of LANL data received by AFWA. Moreover, knowledge of the actual spacecraft materials used on monitored spacecraft would greatly aid in nailing down the critical temperatures. Furthermore, such knowledge could help narrow down whether charging played an instrumental role in a spacecraft, or instrument, failure.

5.3   Suggestions for Further Study

Closer examination of the 14 March 1999 charging event could enhance the understanding of the circumstances under which a given distribution function (kappa or Maxwellian) gives the best results. Along this line, closer scrutiny might also aid in understanding why LANL 1994-084 data fit more quickly, and definitely, to the kappa distribution than either 1991-080 or 1997A. Recall that the data from these latter two data sets were similar, but distinctly different from the 1994-084 data, in that the high and low potential plots showed a tendency toward fitting with Maxwellian distributions.

Extending the study to additional cases would help broaden the basis for comparison of the distribution functions. Such further examination could help to generalize, or refine, conclusions made in this research.

The present research is restricted to an assumption of normal incidence. Broadening the formulation of the current balance equation to include angle-dependent secondary and backscattered coefficients would aid in analysis of "dwell time" near the surface, allowing for more secondaries to be produced (Hastings and Garrett, 1996:150). The coefficients for isotropic incidence are made available by Lai (1991:1630-1631).

Hellberg and Mace (2002) discuss the benefits of using a kappa-Maxwellian distribution in plasma dispersion functions. Due to the anisotropy of space plasmas, using the kappa distribution in a parallel temperature relation and the Maxwellian in the perpendicular could possibly result in a more inclusive fit. The applicability of

this approach to current balance has not been investigated and is merely a suggestion for consideration. However, since LANL instruments take parallel and perpendicular electron temperature measurements, there may be some applicability.

Concurrent with increased charging, the forbidden region becomes evident, and the high-energy tail distribution increases. This brings about an "elbow" at the cut off point. There is currently no explanation for this, so the significance of this feature, if any, is undetermined. The presence of this "elbow" is highlighted in Section 4.2.

Appendix A. Determination of Eclipse Periods for Spacecraft in

Geosynchronous Orbit

The LANL data examined for this research provided spacecraft location in terms of geographic coordinates (GEO). The GEO coordinate system is the same as that used to identify locations on Earth (latitude and longitude). This system is oriented with respect to the earth's spin axis and equator. However, the coordinate system reported in the LANL data is spacecraft centered (Thomspen, et al., 1999:19), so the reported values must be divided by R_E.

As per a suggestion by Michelle Thomsen of the Los Alamos National Laboratory, the procedure for determining whether or not a spacecraft is in eclipse is to convert the spacecraft location coordinates from GEO to GSM (see, for example, Kivelson and Russell, 1995:Appendix 3) and verify if SQRT(YGSM^2 + ZGSM^2) < 1 (personal correspondence between M. Thomsen and D. Della-Rose, November 2002). This appeared to work well since the times determined to be eclipse periods were near spacecraft local midnight.

The geocentric solar magnetospheric system (GSM) is oriented with respect to the earth-sun line and the earth's magnetic dipole (though, not parallel to this dipole) which is offset from the spin axis by about 11° latitude. The critical difference that makes this system useful for determining eclipse is that the satellite will be opposite the sun in the plane of the earth-sun line at equatorial latitudes near equinox and, therefore, in the earth's shadow. In addition to the criteria mentioned above, it was necessary to ensure the spacecraft was not on the dayside of its orbit since the critical criteria SQRT(YGSM^2 + ZGSM^2) < 1 occurred both in the noon and midnight sectors.

The verification of the criteria SQRT(YGSM^2 + ZGSM^2) < 1 was accomplished by converting GEOPACK (Tsyganenko, 2001) library FORTRAN code into MATLAB$^{\circledR}$ (with modifications specific to the problem at hand). GEOPACK is a

software package designed to aid scientists in converting among various space physics related coordinate systems for research and analysis purposes.

The output was imported into Mathcad[R] and graphically incorporated into Figures 2 and 3 as well as similar figures in following sections.

Appendix B. Development of the kappa Current Balance Equation Using the Whittaker Function

Consider the integral representation of the *kappa* current balance equation:

$$\int_0^\infty \varepsilon f(\varepsilon) d\varepsilon = \int_0^\infty \varepsilon f(\varepsilon)[\delta(\varepsilon) + \eta(\varepsilon)] d\varepsilon \tag{36}$$

$$\int_0^\infty \varepsilon \left[1 + \frac{\varepsilon}{\left(\kappa - \frac{3}{2}\right) T_\kappa}\right]^{-(\kappa+1)} d\varepsilon$$

$$= \int_0^\infty \varepsilon \left[1 + \frac{\varepsilon}{\left(\kappa - \frac{3}{2}\right) T_\kappa}\right]^{-(\kappa+1)} \{c[e^{-\varepsilon/a} - e^{-\varepsilon/b}] + A - Be^{-\varepsilon C}\} d\varepsilon \tag{37}$$

where we note that the normalization constants divide out.

Recall that $\kappa > 3/2$. For the left hand side, set

$$x = \frac{\varepsilon}{\left(\kappa - \frac{3}{2}\right) T_\kappa} \qquad \text{and} \qquad dx = \frac{d\varepsilon}{\left(\kappa - \frac{3}{2}\right) T_\kappa}$$

$$\int_0^\infty \varepsilon \left[1 + \frac{\varepsilon}{\left(\kappa - \frac{3}{2}\right) T_\kappa}\right]^{-(\kappa+1)} d\varepsilon = \left[\left(\kappa - \frac{3}{2}\right) T_\kappa\right]^2 \int_0^\infty x \left[1 + x\right]^{-(\kappa+1)} dx \tag{38}$$

Now use integration by parts with

$$u = x \qquad\qquad du = dx$$

$$v = \frac{[1+x]^{-\kappa}}{-\kappa} \qquad\qquad dv = [1+x]^{-(\kappa+1)} dx$$

to yield

$$\int_0^\infty \varepsilon \left[1 + \frac{\varepsilon}{\left(\kappa - \frac{3}{2}\right) T_\kappa}\right]^{-(\kappa+1)} d\varepsilon = \frac{\left[\left(\kappa - \frac{3}{2}\right) T_\kappa\right]^2}{\kappa(\kappa - 1)} \tag{39}$$

which is also the coefficient of A on the right hand side of the equation.

With $\alpha = 1/a$, $1/b$, or C as applicable, for the right hand side, set

$$c - a - 1 = -(\kappa + 1) \qquad\qquad a - 1 = 1$$

$$c - a = -\kappa \qquad\qquad a = 2$$

$$c - 2 = -\kappa$$

$$c = 2 - \kappa$$

$$u = \varepsilon\alpha \qquad\qquad z = \left(\kappa - \tfrac{3}{2}\right) T_\kappa \alpha$$

Substituting these values into the Whittaker function (Morse and Feshbach, 1954:612,672):

$$U_2(a|c|z) = \frac{e^{ia\pi} z^{-a}}{\Gamma(a)} \int_0^\infty e^{-u} u^{a-1} \left[1 + \frac{u}{z}\right]^{c-a-1} du \tag{40}$$

and we note that $a = 2$ yields

$$e^{i2\pi} z^{-2} = z^{-2}$$

$$\Gamma(2) = 1$$

and apply this term by term except for A. We get

$$\int_0^\infty e^{-\varepsilon\alpha} \varepsilon\alpha^{2-1} \left[1 + \frac{\varepsilon\alpha}{\left(\kappa - \tfrac{3}{2}\right) T_\kappa \alpha}\right]^{2-\kappa-2-1} d\left(\varepsilon\alpha\right)$$

$$= \alpha^2 \int_0^\infty e^{-\varepsilon\alpha} \varepsilon \left[1 + \frac{\varepsilon}{\left(\kappa - \tfrac{3}{2}\right) T_\kappa}\right]^{-(\kappa+1)} d\varepsilon \tag{41}$$

$$= \left[\left(\kappa - \frac{3}{2}\right) T_\kappa \alpha\right]^2 U_2(2|2 - \kappa|\left(\kappa - \frac{3}{2}\right) T_\kappa \alpha) \tag{42}$$

69

Therefore,

$$\int_0^\infty e^{-\varepsilon\alpha}\varepsilon \left[1 + \frac{\varepsilon}{\left(\kappa - \frac{3}{2}\right)T_\kappa}\right]^{-(\kappa+1)} d\varepsilon = \left[\left(\kappa - \frac{3}{2}\right)T_\kappa\right]^2 U_2(2|2 - \kappa| \left(\kappa - \frac{3}{2}\right)T_\kappa\alpha) \tag{43}$$

Finally, replace α with $1/a$, $1/b$, or C representing the terms on the right hand side. Now set the left hand side equal to the right hand side and simplify to get

$$\kappa(\kappa - 1)\{c[U_2(2|2 - \kappa| \left(\kappa - \frac{3}{2}\right)\frac{T_\kappa}{a}) - U_2(2|2 - \kappa| \left(\kappa - \frac{3}{2}\right)\frac{T_\kappa}{b})]$$
$$-BU_2(2|2 - \kappa| \left(\kappa - \frac{3}{2}\right)T_\kappa C)\} + A - 1$$
$$= \quad 0 \tag{44}$$

The solution T_κ of this equation, for a given κ, is the critical temperature for the onset of spacecraft charging.

Appendix C. (Partial) Table of Channel Energies

Edge No.	elec 080	Ectr e080	elec 084	Ectr e084	elec 97A	Ectr e97A
0	46375		47135		47539	
1	35412	40522	35849	41107	36214	41492
2	27041	30944	27266	31264	27586	31607
3	20648	23629	20737	23778	21014	24077
4	15767	18043	15772	18085	16008	18341
5	12040	13778	11995	13755	12194	13971
6	9193.5	10521	11995	10461	9289	10643
7	7020.2	8033.7	9123.2	7956.4	7076	8107.4
8	5360.6	6134.5	6938.8	6051.3	5390.3	6175.9
9	4093.4	4684.3	5277.3	4594.5	4106.1	4704.6
10	3120	3573.7	4000	3492.8	3100	3567.8

Table 1   (Partial) Table of Channel Energies

Appendix D.   Critical Temperatures for non-activated CuBe

κ	T_c
2.5	1.712
3.5	1.519
4.5	1.457
5.5	1.427
6.5	1.4097
7.5	1.397
8.5	1.389
9.5	1.383
10.5	1.378
11.5	1.374
12.5	1.371
13.5	1.369
14.5	1.367
15.5	1.365
16.5	1.363
17.5	1.362

Table 2   Critical Temperatures for CuBe (non-activated) with kappa = 2.5 to 17.5

Bibliography

Abramowitz, Milton and Irene A. Stegun, eds. *Handbook of Mathematical Functions.* Washington, DC: National Bureau of Standards, 1964.

Carpenter, D. L. "Whistler Evidence of a 'Knee' in the Magnetospheric Ionization Density Profile." *Journal of Geophysical Research,* 68 (No. 6):1675-1682 (March 1963).

Christon, S. P. and others. "Energy Spectra of Plasma Sheet Ions and Electrons from 12650 eV/e to 1261 MeV During Plasma Temperature Transitions." *Journal of Geophysical Research,* 93 (No. A4):2652-2572 (April 1988).

DeForest, Sherman E. "Spacecraft Charging at Synchronous Orbit." *Journal of Geophysical Research,* 19:577-616 (November 1981).

Gringauz, K. I. "The Structure of the Ionized Gas Envelope of Earth from Direct Measurements in the USSR of Local Charged Particle Concentrations." *Planetary and Space Science,* 11:281-296 (1963).

Hastings, Daniel and Henry Garrett. *Spacecraft-Environment Interactions.* Cambridge: Cambridge University Press, 1996.

Kivelson, Margaret G. and Christopher T. Russell, eds. *Introduction to Space Physics.* Cambridge: Cambridge University Press, 1995.

Lai, Shu T. "Spacecraft Charging Thresholds in Single and Double Maxwellian Space Environments." *IEEE Trans on Nuclear Science.,* 38:1629-1634 (December 1991).

Lai, Shu T. "Lectures on Spacecraft Charging and Mitigation." Graduate School Programme, Space Physics Department, Umea University, Kiruna, Sweden, September/October 1999.

Lai, Shu T. and Devin J. Della-Rose. "Spacecraft Charging at Geosynchronous Altitudes: New Evidence of the Existence of Critical Temperature." *Journal of Spacecraft and Rockets,* 38 (No. 6): 922-928 (November/December 2001).

Lai, Shu T. and M. Tautz. "Critical Temperature for the Onset of Spacecraft Charging at Geosynchronous Altitudes: A Statistical Study." *EOS Trans. AGU,* 83(19), Spring Meet. Suppl., Abstract SM52A-12, 2002.

Hellberg, M.A. and R.L. Mace. "Generalized Plasma Dispersion Function for a Plasma with a kappa-Maxwellian Velocity Distribution." *Physics of Plasmas,* Vol. 9 (No. 5):1495-1504 (May 2002).

Meyer-Vernet, Nicole: "How Does the Solar Wind Blow? A Simple Kinetic Model." *European Journal of Physics,* 20: 167-176 (February 1999).

Meyer-Vernet, Nicole: "Large Scale Structure of Planetary Environments: The Importance of Not Being Maxwellian." *Planetary and Space Science*, 49: 247-260 (May 2001).

Morse, Philip M. and Herman Feshbach. *Methods of Theoretical Physics.* New York: McGraw-Hill Book Company, 1953.

Parks, George K. *Physics of Space Plasmas.* Reading, MA:Perseus Books, 1991.

Prokopenko, S. M. L. and J. G. Laframboise. "High-Voltage Differential Charging of Geostationary Spacecraft." *Journal of Geophysical Research*, 85 (No. A8): 4125-4131 (August 1980).

Rubin, A., Garrett, H. B., and A. H. Wendel: "Spacecraft Charging on ATS-5." Air Force Geophysics Laboratory, AFGL-TR-80-0168, AD-A090508, 1980.

Sanders, N. L. and G. T. Inouye. "Secondary Emission Effects on Spacecraft Charging: Energy Distribution Considerations." *Spacecraft Charging Technology1978*, Ed. R. C. Finke and C. P. Pike. 747-755, Air Force Geophysics Laboratory. NASA-2071, AD-A084626, 1978.

Sternglass, Ernest J. "Backscattering of Kilovolt Electrons from Solids." *Physical Review*, 95 (No.2):345 (July 1954).

Su, Yi-Jiun and others. "Plasmaspheric Observations at Geosynchronous Orbit." *Journal of Atmospheric and Solar-Terrestrial Physics*, 63:1185-1197 (July, 2001).

Summers, Danny and Richard M. Thorne. "The Modified Plasma Dispersion Function." *Physics of Fluids B*, Vol. 3 (No. 8):1835-1847 (August 1991).

Thomsen, Michelle and others. "Calculation of Moments from Measurements by the Los Alamos Magnetospheric Plasma Analyzer." Los Alamos National Laboratory. LA-13566-MS, May 1999.

Tsyganenko, N. A. "GEOPACK." FORTRAN Subroutines: SUN, RECALC, GEOGSM. http://www-spof.gsfc.nasa.gov/Modeling/geopack.html. 27 November 2002.

Vasyliunas, Vytenis M. "A Survey of Low-Energy Electrons in the Evening Sector of the Magnetosphere with OGO 1 and OGO 3." *Journal of Geophysical Research*, 73 (No. 9): 2839-2884 (May 1968).

Vita

Capt Harris entered service in the United States Air Force in 1984. He served as a Russian linguist before obtaining a commission through the Air Force Airman Education and Commissioning Program in 1995. During the program, he earned a B.S. in Meteorology and one in Mathematics at The Florida State University.

As an Air Force weather officer, he has served at Mountain Home AFB, ID (366 OSS/OSW); Camp Red Cloud, ROK (Det 2, 607WS); and Shaw AFB, SC (28 OWS). He authored this thesis as a student at the Air Force Institute of Technology, Wright-Patterson AFB, OH. His follow-on assignment is to Offutt AFB, NE.

1. REPORT DATE *(DD-MM-YYYY)*	2. REPORT TYPE	3. DATES COVERED *(From – To)*
25-03-2003	**Master's Thesis**	Aug 2001 – Mar 2003

4. TITLE AND SUBTITLE

SPACECRAFT CHARGING AT GEOSYNCHRONOUS ALTITUDES: CURRENT BALANCE AND CRITICAL TEMPERATURE IN A NON-MAXWELLIAN PLASMA

5a. CONTRACT NUMBER

5b. GRANT NUMBER

5c. PROGRAM ELEMENT NUMBER

6. AUTHOR(S)

Harris, Jose T., Captain, USAF

5d. PROJECT NUMBER

5e. TASK NUMBER

5f. WORK UNIT NUMBER

7. PERFORMING ORGANIZATION NAMES(S) AND ADDRESS(S)
Air Force Institute of Technology
Graduate School of Engineering and Management (AFIT/EN)
2950 Hobson Street, Building 640
WPAFB OH 45433-7765

8. PERFORMING ORGANIZATION REPORT NUMBER

AFIT/GAP/ENP/03-05

9. SPONSORING/MONITORING AGENCY NAME(S) AND ADDRESS(ES)
HQ AFWA/XOGX
106 Peacekeeper Dr
Suite 2N3
Offutt AFB, NE 68113-4039

10. SPONSOR/MONITOR'S ACRONYM(S)

11. SPONSOR/MONITOR'S REPORT NUMBER(S)

12. DISTRIBUTION/AVAILABILITY STATEMENT

APPROVED FOR PUBLIC RELEASE; DISTRIBUTION UNLIMITED.

13. SUPPLEMENTARY NOTES

14. ABSTRACT

Spacecraft charging threatens to disable spacecraft components and adversely impact any satellite function. Electrostatic charge, and especially discharge, can hinder the proper operation of, or destroy, spacecraft components, thereby rendering the spacecraft ineffective or inoperative (Prokopenko and Laframboise, 1980:4125). The level of charging is dependent on the particle energy (speed) distribution. Current spacecraft design and materials provide limited protection against the dangers of electrostatic discharge, and active measures such as beam emission are also employed. The goal of this thesis is to investigate the kappa distribution as an alternative to the Maxwellian distribution as a method of predicting the onset of significant spacecraft charging by extending the research of Lai and Della-Rose (2001). Their work demonstrated the existence of critical (electron) temperatures above which the onset of significant spacecraft charging occurs. Below this critical temperature, significant charging does not occur (Lai and Della-Rose, 2001:927).

Space plasmas are known to exhibit non-Maxwellian distributions at high (>10 keV) energies (Vasyliunas, 1968:2840), and this knowledge provides the motivation for extending the work of Lai and Della-Rose to the kappa distribution. Solving the current balance equation is central to this area of research. Data from Los Alamos National Laboratory scientific instruments onboard geosynchronous satellites were analyzed to determine the efficacy of the kappa approach. However, the results of this thesis suggest that the kappa distribution, though superior to the Maxwellian at modeling high-energy particles (electrons), may be no better at determining charging onset.

15. SUBJECT TERMS
Spacecraft Surface Charging, Non-Maxwellian Plasma Distribution, Geosynchronous Satellite, kappa Distribution

16. SECURITY CLASSIFICATION OF:			17. LIMITATION OF ABSTRACT	18. NUMBER OF PAGES	19a. NAME OF RESPONSIBLE PERSON
a. REPORT	**b. ABSTRACT**	**c. THIS PAGE**			Devin J. Della-Rose, Maj, USAF (ENP)
U	U	U	UU	92	**19b. TELEPHONE NUMBER** *(Include area code)* (937) 255-3636, ext 4514; e-mail: devin.della-rose@afit.edu

Standard Form 298 (Rev. 8-98)
Prescribed by ANSI Std. Z39-18